Supporting Information

A classical view on nonclassical nucleation

Paul J. M. Smeets[a,b,c,d], Aaron R. Finney[e,f,g], Wouter J. E. M. Habraken[a,b,h], Fabio Nudelman[a,b,i], Heiner Friedrich[a,b], Jozua Laven[a,b], James J. De Yoreo[j,k], P. Mark Rodger[e,f], and Nico A. J. M. Sommerdijk[a,b,c]

[a]Laboratory of Materials and Interface Chemistry, Department of Chemical Engineering and Chemistry, Eindhoven University of Technology, 5600 MB Eindhoven, The Netherlands; [b]Center for Multiscale Electron Micoscopy, Department of Chemical Engineering and Chemistry, Eindhoven University of Technology, 5600 MB Eindhoven, The Netherlands; [c]Institute for Complex Molecular Systems, Eindhoven University of Technology, 5600 MB Eindhoven, The Netherlands; [d]Department of Materials Science and Engineering, Northwestern University, Evanston, IL 60208; [e]Centre for Scientific Computing, University of Warwick, Coventry CV4 7AL, United Kingdom; [f]Department of Chemistry, University of Warwick, Coventry CV4 7AL, United Kingdom; [g]Department of Materials Science and Engineering, University of Sheffield, Sheffield S1 3JD, United Kingdom; [h]Department of Biomaterials, Max Planck Institute of Colloids and Interfaces, Research campus Golm, D-14424, Potsdam, Germany; [i]EaStCHEM, School of Chemistry, The King's Buildings, University of Edinburgh, Edinburgh EH9 3FJ, United Kingdom; [j]Physical Sciences Division, Pacific Northwest National Laboratory, Richland, WA 99352; [k]Department of Materials Science and Engineering, University of Washington, Seattle, WA 98195.

Table of Contents

1. Materials and Methods

1.1 Chemicals and Solution Preparation

All the solutions were freshly prepared for every experiment utilizing fresh Milli-Q water (resistivity 18.2 MΩ·cm at 20 °C), degassed overnight with N_2. Aqueous NaOH (10 mM) and $CaCl_2$ (10 mM) solutions were prepared by dissolving NaOH pellets (≥ 98%, anhydrous, Sigma S8045), and $CaCl_2 \cdot 2H_2O$ (≥ 98%, Sigma-Aldrich 22350-6) into the degassed water. 10 mM HCl was prepared by dilution of HCl 25% (Merck 100316). A 10 mM carbonate buffer set at pH = 9.75 was prepared by mixing 10 mM Na_2CO_3 (anhydrous, Merck 106392) and 10 mM $NaHCO_3$ (GR for analysis, Merck 106329) to reach the desired pH-value.

1.2 The Principal Titration Set-up

A titration set-up (Metrohm) running Tiamo 1.2 software for constant pH titration was used, including Metrohm accessories (see Gebauer *et al*. (1)). Briefly, a double junction micro pH glass electrode (reference, No. 6.0234.100) containing 3 M KCl electrolyte solution, and a polymer membrane (PVC) calcium (No. 6.0508.110) or sodium (No. 6.0508.100) ion-selective electrode (ISE) were used, connected to two 809 dosing devices, controlling a total of four 800 dosing units.

1.3 Calibration of the pH and Ion Selective Electrodes

Calibration of the pH electrode was done using pH = 4.0 (No. 6.2307.100), pH = 7.0 (No. 6.2307.110) and pH = 9.0 (No. 6.2307.120) Metrohm buffers. The Ca^{2+} (1) and Na^+ (2) ISE were calibrated before each measurement.

(1) Calibration of the Ca^{2+}-ISE: The pH of the 10 mM $CaCl_2$ solution (25 mL) was adjusted to 9.75 by addition of 10 mM NaOH. Next, the Ca^{2+}-ISE was calibrated by addition of the $CaCl_2$ into 25 mL degassed water at an addition speed of 10 $\mu L\ min^{-1}$. Here, the pH was maintained by titrating in 10 mM NaOH and 10 mM HCl while N_2 was gently flown over the solution at constant rate to diminish the influx of CO_2.

(2) Calibration of the Na^+-ISE: The general procedure described for calibration of the Ca^{2+}-ISE was adopted, however, 1.0 M aqueous NaCl was used instead of 10 mM $CaCl_2$. The calibration was performed in the same concentration range as the precipitation experiments to ensure reliable measurements.

1.4 Calcium Carbonate Precipitation Experiments

Experiments were performed at 20 ± 1 °C in a beaker containing a 25 mL 10 mM carbonate buffer. To this buffer, the 10 mM $CaCl_2$ solution (pH 9.75) was dosed at 10 $\mu L\ min^{-1}$, keeping the pH constant by the titration of 10 mM NaOH solution. The Ca^{2+} and Na^+ potentials were measured using the Ca^{2+}-ISE and Na^+-ISE to determine the respective ion concentrations. After every experiment, electrodes, dosing tips and beakers were cleaned with 10% acetic acid and rinsed with distilled water.

1.5 Dynamic Light Scattering (DLS) Measurements

DLS measurements were performed using a Nano ZS ZEN 3600 Zetasizer (Malvern instruments) using a He-Ne laser (λ = 632.8 nm) at 20 °C. Each sample taken along the titration curve was analyzed in a disposable 1 mL cuvette. Dispersion viscosity was 1 mPa·s (water), and for the growing $CaCO_3$ the refractive index for calcite was applied ($n \approx 1.66$). Data analysis was performed using Malvern Zetasizer Software 6.01.

1.6 *In situ* ATR-FTIR Characterization

A Varian 670 FTIR Spectrometer was used in combination with an internal ATRMax II Variable Angle Horizontal ATR (Pike Technologies). The FTIR contained a high intensity ceramic IR-source in combination with a KBr beam splitter. The detector was a photoconductive mercury cadmium telluride (MCT), cooled by liquid nitrogen. All spectra were recorded with a resolution of 2 cm^{-1}. Samples of ~1 mL were taken over time in the titration experiment and analyzed at atmospheric air conditions and 20 ± 1°C. The ATR accessory was set at an incident angle of 45°. The buffer spectrum was created using degassed water as a background spectrum. Further samples were recorded taking a freshly prepared buffer sample as background.

1.7 Light Microscopy Studies

A small aliquot (~0.5 mL) of the solution during the titration experiment was taken at specific time points and immediately transferred onto a glass slide, which was then imaged in the light microscope. Specifically, for light microscopy studies a Polyvar MET Optical Microscope in combination with a photo controller was used in transmission mode. A polarizing filter was attached for visualizing birefringence behavior of $CaCO_3$. The camera was a Colorview Soft Imaging System (Olympus) and software included analySIS 5.0.

1.8 SEM Characterization

For fast and relatively low resolution imaging, a FEI Phenom was used. For this, a sample was taken from solution, put on carbon tape and air-dried for a day. Subsequently it was sputter coated with a layer of gold applying a current coating of 20 mA for a duration of 3 min. Higher magnification SEM images were recorded using a Quanta 3D FEG (FEI, The Netherlands) with a field emission electron gun at 5 kV and a current between 1.48-2.96 pA.

1.9 Cryo-TEM Analysis

Sample vitrification was carried out using an automated vitrification robot (FEI Vitrobot™ Mark III). Sample supports, type R2/2 Quantifoil Jena, were purchased from Quantifoil Micro Tools GmbH and contained a carbon support film on a copper grid. Prior to use the TEM grids were glow discharged by a Cressington 208 carbon coater to render them hydrophilic. Cryo-samples were prepared from a 3 μL droplet of sample solution placed on the grid inside the Vitrobot™ chamber at 100% relative humidity and temperature of 20 °C, after which it was blotted to remove excess solution (blotting time 2 s, blot offset –2) and subsequently plunged into liquid ethane for vitrification.

For imaging of the cryo-samples, two different TEMs were used. A Titan Krios™ (FEI) equipped with a field emission gun (FEG) and operating at 300kV was used for high resolution imaging in the prenucleation stage. Image recording was performed using a 4k by 4k Eagle CCD camera. Second, imaging of larger aggregate structures and low dose selected area electron diffraction (LDSAED) after the prenucleation stage were performed on a FEI Tecnai G2 operated at 200 kV and equipped with a LaB_6 filament. A Gatan cryo-holder operated at approx. -170°C was used and images were recorded with a 1k by 1k pixel Gatan CCD camera.

1.9.1 Analysis of clusters from acquired cryo-TEM images using MATLAB

During the prenucleation stage, cryo-TEM samples were analyzed for the presence of prenucleation species. Hereto we used the Titan Krios^{TM} (FEI, Eindhoven) for being the most powerful microscope available in terms of resolution, detector sensitivity and detector size (4k × 4k pixels CCD). Of importance is the applied defocus value to interpret the nanosized particles. We set a nominal defocus of –0.5 µm to tune the phase-contrast transfer function (CTF) of this microscope to balance good phase contrast and a high directly interpretable resolution (2) of 0.9 nm. Therefore, the proposed particle size distribution for $CaCO_3$ prenucleation clusters (~0.7–2 nm) under these conditions would be detectable (3, 4). Thus, in principle we should be able to observe particles >0.9 nm in thin specimen layers (2).

The obtained images were analyzed using a MATLAB script, as described below.

To test if a global binarization threshold is warranted, the intensity gradient in the images was checked by applying an extremely heavy smoothing operation, removing any contrast arising from smaller features and leaving only a background intensity. The MATLAB function 'imguidedfilter' was used (kernel size 200 pixels) with the same image as the guiding image for this. While this filter is regularly used for edge-preserving smoothing, by selecting a sufficiently high degree of smoothing this feature was disabled. The variation in intensity in the smoothed image was found to be smaller than the standard deviation of the original image. Therefore, it was concluded that the background intensity variations are insignificantly small.

The mean intensity $\bar{I}$ and corresponding standard deviation σ of the original images were calculated. The 2.5% most intense dark pixels in the TEM image (i.e. 2σ) are selected by thresholding, *i.e.* a binary image is created from the grayscale image. Thus, every pixel with an intensity, I_{sig}, lower than $\bar{I}-2\sigma$ becomes the white phase in the created binary image (see Scheme 1c). The criterion for the signal-to-noise ratio (SNR) we apply is SNR = $\left(\bar{I} - I_{\mathrm{sig}}\right)/\ \sigma > 2$.

From the binary image generated, all segmented pixels are described as objects with a connectivity of 8, *i.e.* a criterion for discerning whether objects are connected or separated. Using the 'regionprops' function, every separate object obtained has been analyzed for its equivalent circular diameter (d_{eq}) given by $2\sqrt{\#\text{pixels}/\pi}$, which specifies the diameter of a circle with the same area as the region of pixels of an individual object (Scheme 1d). As dynamically ordered liquid-like oxyanion polymers (DOLLOPs) have been reported with non-spherical structures (5), our approach of using d_{eq} ensures low contrast pixels in objects of irregular shape when measuring a direct diameter is avoided. A histogram of segmented object sizes was produced, from which analysis of larger, low intensity particles can be analyzed (Scheme 1e).

The threshold objects selected were colored opaque green and overlaid on the original image in an area of 25 × 25 pixels (2.92 × 2.92 nm). A red circle was then added around the object with the geometric center (centroid) overlapping with the middle of the circles' diameter. The objects were finally ordered from largest to smallest in the output. No further assumptions, other than the thresholding value set (SNR > 2), were made in the analyses.

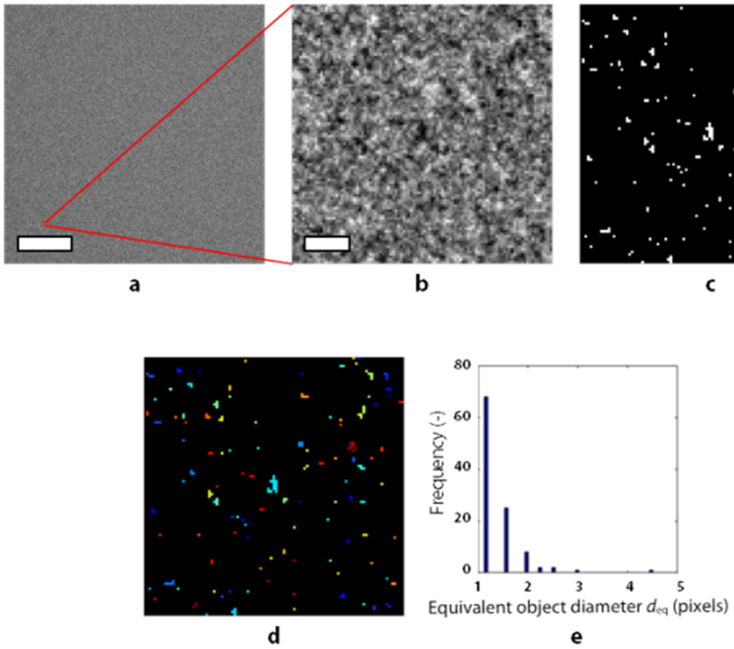

***Scheme S1*. Prenucleation particle analysis procedure using MATLAB. (a)** original TEM image, **(b)** enlarged portion of the image in (a), **(c)** binary image of (b) with darkest pixels segmented, **(d)** color-labeled image according to individual object size of (c), and **(e)** equivalent diameter (d_{eq}) distribution of objects. Scale bars (a) 100 nm, (b) 2 nm.

1.9.2 Low-dose Selected Area Electron Diffraction

LDSAED was performed on a FEI Tecnai 20 (type Sphera) TEM. The obtained diffraction patterns were radially averaged to produce a radial intensity profile. In Digital Micrograph™, the center of the diffraction pattern was determined using the DiffTools add-on package. This center was inserted into ImageJ, which was used to produce a profile plot of normalized integrated intensities around concentric circles (the beamstopper was not integrated and thus cancelled out) as a function of the distance from the diffraction rings to the center. Thus, following this procedure, eventually the *d*-spacing of the reflections was determined.

1.10 Simulations Setup

Two types of solution systems were simulated: "random" and "cluster". Here, the system name describes the arrangement of ions in the initial configuration. The details of simulations are provided in Table S1 and Table S2.

Random solutions were prepared by randomly populating a cubic simulation cell with Ca^{2+}, CO_3^{2-} and HCO_3^- ions, such that the distance between any two ions was > 5 Å. The box was then filled with pre-equilibrated water which conserved target concentrations in the millimolar regime. From the total number of cations and anions the total concentrations for calcium, $c(Ca^{2+})$, and (bi)carbonate, $c(C)$, were calculated. The $c(CO_3^{2-})/c(HCO_3^-)$ ratio was used to define pH using the Henderson–Hasselbach equation. The total number of each ion type remained fixed throughout the simulation.

For cluster systems, several thousands of cluster configurations were generated from random structure searches of ions in vacuum, followed by sampling according to cluster radius of gyration, coordination numbers and potential energy order parameters (for a full description, see ref. (6)). From these, a number of low energy clusters spanning a range of densities were identified and used in subsequent calculations. Low energy clusters were extracted with a structure consistent with low density liquid-like clusters, which has been shown as a stable form of calcium carbonate in aqueous solution (7). The extracted clusters were solvated using the same protocol as for the random systems by embedding in pre-equilibrated water.

The force field employed was that of Demichelis *et al*. (7), with intermolecular potentials tapered to zero between 6.0 and 9.0 Å as required, and with SPC/Fw water (8). This force field accurately models the free energies of ion solvation, crucial for the current exercise. Unless otherwise stated, Molecular Dynamics (MD) simulations were performed in the *NpT* ensemble at 298 K and 1 atm with a Nosé–Hoover thermostat (0.1 ps relaxation constant) and barostat (1 ps relaxation constant), and electrostatics were treated using the smooth particle mesh Ewald method with precision 10^{-7}, and with cubic periodic boundaries employed. The timestep was 1 fs, and calculations were performed using DL_POLY 4.05 (9).

Simulations at the lowest concentrations were run for 20 ns for systems at basic pH and up to ~60 ns for all-carbonate cluster systems, with equilibrium averages taken from the final two ns of simulation. Equilibrium was taken as the time after which cluster size distributions and coordination probabilities, as well as energetic and volume averages, remained unchanged within statistical uncertainty on the nanosecond timescale. Equilibrium concentrations were calculated from the total number of free ions in solution, averaged over the final 2 ns windows of trajectories.

Table S1. Initial and final concentrations, and pH for a range of solution and cluster simulations at moderate supersaturation at 298 K containing n_{Carb} carbonate, n_{Bicarb} bicarbonate, n_{Ca} calcium ions, and n_{Wat} water molecules. Uncertainties of one standard deviation in the data are shown in parentheses.

System composition					***t* = 0**			**Equilibrium averages**		
Type	n_{Ca}	n_{Carb}	n_{Bicarb}	n_{Wat}	***c*(C) /mM**	***c*(Ca^{2+}) /mM**	**pH**	***c*(C) /mM**	***c*(Ca^{2+}) /mM**	**pH**
cluster	14	6	16	24424	50.5	32.1	9.90	23.8 (1.4)	3.3 (1.2)	8.4 (0.7)
cluster	20	20	0	55510	20.2	20.2	-	-	-	-
cluster	20	20	0	37006	30.4	30.4	-	-	-	-
cluster	20	20	0	27755	40.5	40.5	-	-	-	-
cluster	20	20	0	22204	50.6	50.6	-	-	-	-
random	14	6	16	24424	50.5	32.1	9.90	26.4 (1.3)	5.1 (2.4)	7.8 (1.2)
random	29	12	34	83132	31.0	19.6	9.88	16.4 (0.7)	4.5 (0.8)	7.4 (1.5)
random	47	30	34	100000	35.9	26.4	10.27	15.5 (0.6)	2.9 (0.4)	8.3 (0.8)

To investigate the formation of dense liquids, random simulations with initial concentrations 0.57 M, 1.1 M and 1.7 M were relaxed at 298 K and 1 atm in the *NpT* ensemble over 60 ns. Subsequently, the configuration at the final step was used to spawn *NVT* simulations at 300, 400, 500 and 600 K. 10 ns trajectories were collected with averages measured from the final 5 ns or 2 ns windows in the case of 300 K and higher temperatures, respectively. The details of these simulations are provided in Table S2.

Table S2. Initial and final concentrations, and pH for a range of solution and cluster simulations at higher concentrations at 298 K containing n_{Carb} carbonate, n_{Bicarb} bicarbonate, n_{Ca} calcium ions, and n_{Wat} water molecules. Uncertainties of one standard deviation in the data are shown in parentheses.

System composition					***t* = 0**			**Equilibrium averages**		
Type	n_{Ca}	n_{Carb}	n_{Bicarb}	n_{Wat}	***c*(C) /mM**	***c*(Ca^{2+}) /mM**	**pH**	***c*(C) / mM**	***c*(Ca^{2+}) /mM**	**pH**
random	100	100	0	10000	566	566	-	7.6 (3.0)	1.4 (1.3)	-
random	200	200	0	10000	1131	1131	-	13.7 (6.2)	1.7 (0.8)	-
random	300	300	0	10000	1692	1692	-	20.1 (5.7)	1.6 (1.4)	-

1.11 Analysis of Clusters in Simulations

Simulation trajectories were analyzed at ~0.5 ps intervals. Coordination of calcium to oxygen of carbonate (Ca–OC) in clusters was confirmed if the Euclidean distance between Ca and O was within 3.8 Å, *i.e.* the cut-off criterion was $r_{\mathrm{Ca–OC}} \leq 3.8$ Å. This distance is slightly larger than the position of the minimum after the first peak in Ca–OC radial distribution functions, and serves to reduce the fluctuations in cluster numbers. Calcium to carbon (Ca–C) coordination was calculated for atoms within 4.2 Å: $r_{\mathrm{Ca–C}} \leq 4.2$ Å. Clusters comprising a single ion were described as free ions in solution. The mass weighted average cluster size, S, was determined as

$$S = \frac{\sum s\, W_S}{\sum W_S} \tag{1.1}$$

with s representing the number of atoms in the cluster, W_S the cluster mass and the sum is over all clusters in each configuration. Analysis of cluster properties was performed using an in-house analysis package and trajectories were visualized using VMD (10). A number of cluster properties were calculated as a function of radius; this was measured from the center of mass of relevant Ca^{2+}, CO_3^{2-} and HCO_3^- atoms and was recalculated for each configuration analyzed.

The radius of gyration, R_g, provides an indication of cluster size:

$$R_g^2 = \frac{1}{M}\sum_{i=1}^{N} m_i(\boldsymbol{r}_{\mathrm{i}} - \boldsymbol{r}_{\mathrm{com}})^2 \tag{1.2}$$

Here, N is the number of atoms in the cluster, M is the cluster mass, m_i and $\boldsymbol{r}_{\mathrm{i}}$ are atom masses and coordinates, and $\boldsymbol{r}_{\mathrm{com}}$ is are the coordinates for the cluster centre of mass. At high concentrations, ionic networks were observed to span simulation periodic boundaries in x, y or z, leading to clusters of infinite size. To calculate properties as a function of radius, the cluster was first divided into a number of ~10 Å sections parallel to the dimension of percolation, d_{p}. A center of mass c_{s}, was then calculated for atoms of ions in each section. Properties were measured as a function of radius on a cylindrical cross section, for a cylinder with longitudinal axis through c_{s} and parallel to d_{p}.

The diffusion of calcium and carbon ions within dense liquids was measured from the mean squared displacement as a function of time, t:

$$D = \frac{1}{6}\lim_{t\to\infty}\left(N^{-1}\sum_{i=1}^{N}[\Delta\mathbf{r}_{\boldsymbol{i}}(t) - \Delta\mathbf{R}(t)]^2\right) \tag{1.3}$$

In the above equation, D and N are the diffusion coefficient and number of atoms, respectively. $\Delta\mathbf{r}_i = \mathbf{r}_i(t) - \mathbf{r}_i(0)$, where $\mathbf{r}_i$ are the Cartesian coordinates of atoms in the cluster, while $\Delta\mathbf{R}(t) = \mathbf{R}(t) - \mathbf{R}(0)$, where $\mathbf{R}$ are cluster center of mass coordinates (measured using ion positions at each step, but with cluster membership defined by ions at $t = 0$).

Cluster atoms were assigned to a radial bin from cluster centers of mass (bin width 3.0 Å). As described above, in the case of clusters which percolated through simulation cell boundaries, a number of centers of mass were used to assign atoms to bins. Due to the relatively high mobility of ions, atoms may move in and out of the assigned bins throughout the simulation trajectory. Therefore, bin assignment was performed at step one (*i.e.* each time origin used) and these assignments did not change as time evolved. Furthermore, the center of mass at each analysis step was recalculated according to the positions at time t of atoms identified at step one, ensuring smooth spatial evolution. Diffusion of ions within the phase was calculated from the average diffusion of ions from each radial window during the final 5 ns of 300 K simulations, and 20 ps time origins were used to reduce uncertainties in the data.

1.12 TEM Image Simulations

To compare the properties of dense liquids observed in simulation with those found in experiments, we performed a series of TEM Simulations. Here, we have modified a version of the multislice algorithm of Rullgård *et al.* (11). This method uses a quantum mechanical treatment of electrons interacting with a classically evaluated sample object, summarized here (for full details see Ref. 11). The TEM simulation can be described in three parts: the incident beam, the scattering of the beam by the sample, and electron detection/image formation.

1.12.1 Incident Electron Beam

A stationary model solution to the Schrödinger equation is assumed; hence, the wavefunction, Ψ, of an electron can be written as,

$$\Psi(\mathbf{r},t) = \Psi(\mathbf{r},0)\exp\left(\frac{-\mathrm{i}E_{\Psi}t}{\hbar}\right) \tag{1.4}$$

where $\hbar$ is the reduced Planck constant, $\mathbf{r}$ are spatial coordinates, t is time and E_{Ψ} is energy. TEM can be modelled by considering the effect of the sample on a suitably defined electron wave. The incident wavefunction, Ψ_{in}, is modelled using a plane wave of the form,

$$\Psi_{\text{in}}(\mathbf{r}) = \exp(-\mathrm{i}k\mathbf{r}\omega) \tag{1.5}$$

Here, k is the wavenumber and together with ω defines a plane wave propagating perpendicular to the sample and parallel to the TEM optical axis z.

1.12.2 Electron Scattering

On interaction with the sample, the incident wave is scattered, and this gives rise to phase contrast. The shifted wavefunction Ψ_{sc} is calculated according to the integral of the scattering potential $F(\mathbf{r})$, assuming only high energy electrons,

$$\Psi_{\text{sc}}(\mathbf{r}) \approx \Psi_{\text{in}}(\mathbf{r})\exp\left(-\frac{i}{2k}\int F(\mathbf{r}+t\omega)dt\right) \tag{1.6}$$

where $F(\mathbf{r})$ is directly related to the electrostatic potential V of the sample:

$$F(\mathbf{r}) = \frac{2m_0 e}{\hbar^2}\left(V(\mathbf{r}) + iV_{\mathrm{abs}}(\mathbf{r})\right) \tag{1.7}$$

Here, m_0 and e are the reduced electron mass and charge, respectively. To account for amplitude contrast an imaginary potential, iV_{abs}, is added to model the loss of electrons outside of the microscope aperture. Both models for phase and amplitude contrast are based on the electrostatic potentials of individual atoms. These can be modelled as,

$$V(\mathbf{r}) = \frac{16\pi^{5/2}\hbar^2}{m_0 e}\sum_{i}^{n}\frac{a_i}{b_i^{3/2}}\exp\left(\frac{-4\pi^2|\mathbf{r}|^2}{b_i}\right) + \frac{e\Delta Z}{4\pi\epsilon_0|\mathbf{r}|} \tag{1.8}$$

In the above equation, ϵ_0 is the vacuum permittivity and ΔZ is the ionic charge. For neutral atoms, the final term in equation 1.8 is zero. Parameters a and b can be found by fitting a series of exponential functions to the scattering factors of individual atoms. In the current work, a and b values from Peng and co-workers (12, 13) have been used to model Ca^{2+}, C, O^- and H. The potentials for the entire sample are then approximated as a collection of single atoms.

Two approaches were used to assign charges and electrostatic potentials to carbonate ions, both of which used a +2*e* charge for calcium, and neutral atoms for carbon, oxygen and hydrogen of water. In the first, two oxygen atoms of each carbonate were chosen at random and assigned a -1*e* charge. Tests confirmed that for the simulated samples in the current work, the assignment of charges did not affect the measured electron intensities at the detector. In the second approach, the scattering factors for O and O^- were taken from the work of Peng and co-workers (12, 13) and were interpolated to provide an artificial scattering factor for oxygen with a -0.6667*e* charge. Five exponential functions were fitted to the resulting curve and *a* and *b* parameters were determined; these are provided in Table S3. All oxygen atoms of carbonate were then assigned the same charge and electrostatic potential. The measured intensities for the same sample prepared with both approaches were the same within noise; hence, for the remainder of the work, the data from measurements taken using the second method of charge assignment are presented.

Table S3. Scattering parameters for oxygen with a -0.6667*e* charge, determined by interpolating between the experimental scattering factors for neutral and -1*e* oxygen atoms.

a	***b***
0.2888	0.5809
0.9995	4.3041
1.1936	16.5411
5.3149	63.5524
-4.9243	63.5496

1.12.3 Image Detection

Leaving the sample, the wavefunction immediately above the detector, Ψ_{out}, can be written as,

$$\Psi_{\text{out}}(\boldsymbol{r}) = \mathcal{F}^{-1}[\text{CTF} \cdot \mathcal{F}\Psi_{\text{out}}](\boldsymbol{r}) \tag{1.9}$$

Here, the Contrast Transfer Function, CTF, is applied to the Fourier Transform of the scattered electrons and this determines the phase contrast of the resulting 2D image. The CTF is a function of a number of optical parameters, such as the defocus and spherical aberration (see Rullgård *et al.* for details).

The detector is a 2D plane divided into pixels. The intensity, I, at each pixel is proportional to the probability of finding an electron:

$$I(\boldsymbol{r}) = |\Psi_{\text{out}}(\boldsymbol{r})|^2 \tag{1.10}$$

To account for shot noise a Poisson distribution of this intensity, scaled by the electron dose, is detected in a region of the detector plane. In TEM, correlation of the intensity between nearby pixels is often observed due to, for example, spreading of photons following interaction with incoming electrons at the detector. To model this and other detector blurring phenomena, a convolution of the predefined intensities (scaled according to the detector quantum efficiency and detector gain) with the Fourier Transform of a Modulation Transfer Function (MTF) is performed. MTF parameters were calibrated against experiments.

1.12.4 TEM Sample Preparation

To compare with experimental TEM images, the system at 1.7 M was used to perform TEM simulations. The final configuration was used as input. In this system, ionic networks percolated through the simulation cell boundaries in the *x* dimension, and was further split across simulation *y* and *z* periodic boundaries. To get a clear indication of the electron transmission properties of the ion-rich and water-rich liquids, a 133.1 × 13.3 × 13.3 nm (20 × 2 × 2) supercell was created with the *x*-axis oriented parallel to the optical axis in simulation. This ensured that electrons were transmitted through regions which were rich in ions and water in the entire depth of the sample (see Fig. 5 g main text). It is possible that the periodicity in the supercell introduces an additional contribution to phase contrast that would not be found in true amorphous phases; however, the computational cost of simulating this size system would be too large.

Additional TEM simulations were performed for bulk ACC phases. Here, random distributions of ions (300 $CaCO_3$ units) and a varying number of water molecules ($CaCO_3 \cdot n\, H_2O$ where n = 0–7) were first generated. This was done following a similar procedure to Bushuev *et al.* (14) and involved populating a box at random at low density. The resulting configuration was relaxed at 750 K and 100 atm with electrostatics switched off and with an additional Ca-Ca intermolecular pair potential to avoid calcium close contact. Sequential 0.25 ns simulations were then performed at constant pressure and temperatures of 650 K, 550 K, 450 K and 350 K. Finally, 2 ns MD simulations were performed at 298 K and 1 atm with the full potential reinstated. Radial distribution functions confirmed that all structures were amorphous and densities were consistent with those presented for ACC with the same levels of hydration in previous work (14).

Supercells of the bulk ACC configurations were constructed as 2 × 2 × *nz*, where *nz* was chosen so that the depth of the sample parallel to the optical axis was 130 ± 2 nm.

1.12.5 TEM Simulation Parameters

Unless otherwise stated, the following parameters were used for TEM simulations

Electron Beam	
Acceleration voltage	200 kV
Energy spread	0.7 V
Electron dose	32000 e^{-} nm^{-2}
Optics	
Magnification	200000
Defocus nominal	0.087 μm (Scherzer defocus)
Spherical aberration	2 mm
Chromatic aberration	2 mm
Aperture diameter	10 μm
Focal length	2.7 mm
Aperture angle	0.1 mrad
Detector	
x,y pixels	512
Pixel size	10 μm
Detector gain	6.0 counts per e^{-}
Detector quantum efficiency (DQE)	0.6
MTF a	0.12368
MTF b	0.82842
MTF c	0.005
MTF α	2413.6
MTF β	14.3
MTF p	1
MTF q	1

2. Experimental Calculations and Data

2.1 Titration Experiments and Normalization Procedure

We applied a normalization procedure to compare individual titration experiments, where we chose the time at which the supersaturation reaches a maximum (i.e. a maximum value in the free Ca^{2+} curve; $t_{\sigma\ max}$) as 1 (Fig. S1). With this normalization, we are able to indicate the point of maximum supersaturation and the bending point (BP) during the growth stage.

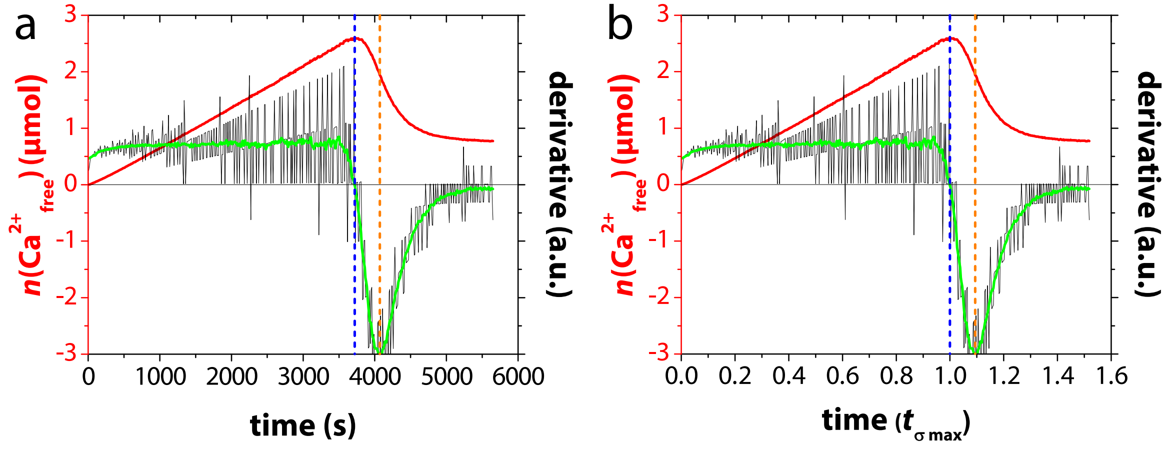

Figure S1. Normalization method for a typical titration experiment. **(a)** The amount of free Ca^{2+} vs. time (red) is shown on the primary y-axis, and its derivative (black) on the secondary y-axis. The latter was smoothed (20 pts; green line) to show where the derivative equals 0 (blue dotted line): $t_{\sigma\ max}$. The orange dotted line indicates the bending point (BP) (min. derivative) in the growth stage. **(b)** Time-normalized image of (b) with $t_{\sigma\ max} = 1$.

2.2 Quantification of $c(Ca^{2+})$ in Titration Experiments

2.2.1 Relating Ca^{2+} potentials to Ca^{2+} concentrations

All $CaCO_3$ precipitation experiment by titration were preceded by an electrode calibration test as described here. For perfectly Nernstian behavior, the calcium activity $a(Ca^{2+})$ and the concentration of free calcium $c(Ca^{2+})$ (4) can be determined from the calcium ion selective electrode (Ca^{2+}-ISE) potential $U(Ca^{2+})$ using (15)

$$U(\mathrm{Ca}^{2+}) = U_0 + s \ln\left[\frac{a(\mathrm{Ca}^{2+})}{c^{\otimes}}\right] = U_0 + s \ln\left[\gamma(\mathrm{Ca}^{2+})\frac{c(\mathrm{Ca}^{2+})}{c^{\otimes}}\right] \qquad (2.1)$$

with $c^{\otimes}$ being the standard concentration, U_0 the electrode intercept, and $s = RT / 2F$, with R the gas constant, T the temperature, and F the Faraday constant. $\gamma(Ca^{2+})$ represents the individual calcium activity coefficient as assessed by using Eq. (2.15). The Ca^{2+}-ISE employed here was calibrated by the measured relation between $a(Ca^{2+})$ and $U(Ca^{2+})$ while adding $CaCl_2$ to water for which the pH was set and held at 9.75 by addition of NaOH. The ISE showed perfect Nernstian behavior over the largest part of the concentration range tested (28.2 mV/decade; compared with the theoretical value of 29 mV at 20 °C); however, at lower concentrations it deviated from Nernstian behavior. As a consequence, from 4×10^{-7} to 2×10^{-4} M, an 8th order polynomial was fitted to the calibration curve of $\ln[a(Ca^{2+})]$ as a function of $U(Ca^{2+})$. This fit was used for the subsequent nucleation by titration experiments to establish calcium activities.

Comparison of the Nernstian slopes for the experiments (in buffered solution) *vs.* the calibration (in pure solution) resulted in similar slopes of 28.2 mV/decade for the detected calcium activity. This confirms that the calcium potentials $U(Ca^{2+})$ are unaffected by the presence of the buffer. Therefore, the presence of Na^+ does not interfere significantly with the measurement of free Ca^{2+} activities in the given setup. According to the manufacturer, 260 mM Na^+ is required to to produce an error of ca. 10 % at 1 mM Ca^{2+}(16).

2.2.2 Determining concentrations of the relevant ions

The ionic strength I in the buffer system can be expressed via

$$I = 0.5 \sum c_i z_i^2 \quad (2.2)$$

with c_i being the molar concentration of the i^{th} ion and z_i its charge. For the titration experiment of the $CaCl_2$ into the $NaHCO_3/Na_2CO_3$ buffer we can write,

$$I = 0.5 \begin{Bmatrix} c(H^+)+c(OH^-)+c(Na^+)+c(Cl^-)+c(HCO_3^-) \\ +(c(CO_3^{2-})\cdot 2^2)+(c(Ca^{2+})\cdot 2^2) \end{Bmatrix} \quad (2.3)$$

and calculate the concentration of different free ions in solution (Eqs. 2.4–2.8) as

$$c(H^+) = \frac{10^{-(pH)}}{\gamma(H^+)}\cdot c^{\otimes} \quad (2.4)$$

$$c(OH^-) = \frac{10^{-(pK_w-pH)}}{\gamma(OH^-)}\cdot c^{\otimes} \quad (2.5)$$

$$c(Na^+) = \frac{2\cdot c(CO_3^{2-})+c(HCO_3^-)+c(NaOH_{add})+c(NaOH_{cal})}{\gamma(Na^+)} \quad (2.6)$$

with $c(NaOH_{add}) = c(NaOH_i)\cdot V(NaOH_{add})/V_{tot}$, the concentration of NaOH added during the experiment, and $c(NaOH_i)$ being the initial NaOH concentration (10 mM); $V(NaOH_{add})$ is the volume of NaOH added to the buffer during the experiment, and V_{tot} is the total volume of solution. $c(NaOH_{cal})$ represents the concentration of NaOH in the solution of $CaCl_2$ at pH 9.75 expressed as $c(\mathrm{NaOH_i})\cdot V(\mathrm{NaOH_{cal}})/V_{tot}$ with $V(\mathrm{NaOH_{cal}})$ being the volume of NaOH necessary to fix the $CaCl_2$ solution at pH 9.75.

$$c(\mathrm{Cl^-}) = 2\cdot c(\mathrm{Ca^{2+}_{add}}) = \frac{2\cdot c(\mathrm{Ca^{2+}_i})\cdot V(\mathrm{Ca^{2+}_{add}})}{V_{\mathrm{tot}}} \tag{2.7}$$

where $c(\mathrm{Ca^{2+}}_{\mathrm{add}})$ and $V(\mathrm{Ca^{2+}}_{\mathrm{add}})$ represent the total increase in calcium concentration and volume on addition of $CaCl_2$ solution to the buffer, respectively, and $c(\mathrm{Ca_i^{2+}})$ is the initial calcium concentration.

$$c(\mathrm{Ca^{2+}}) = \frac{a(\mathrm{Ca^{2+}})}{\gamma(\mathrm{Ca^{2+}})}\cdot c^{\otimes} \tag{2.8}$$

with $a(\mathrm{Ca^{2+}})$ resulting from the measured potential $U_b(\mathrm{Ca^{2+}})$ via Eq. (2.1).

2.2.3 Determining the concentration of carbonate and bicarbonate ions

The concentrations of carbonic acid, bicarbonate and carbonate in the buffer system can be expressed as

$$c(\mathrm{C_{tot}}) = c(\mathrm{H_2CO_3}) + c(\mathrm{HCO_3^-}) + c(\mathrm{CO_3^{2-}}) + c(\mathrm{CO_2}) \tag{2.9}$$

where $c(\mathrm{C_{tot}})$ = 10 mM. The equilibrium of $\mathrm{HCO_3^-} \rightleftarrows \mathrm{CO_3^{2-}} + \mathrm{H^+}$ (pKa_2 of 10.33) (17) dominates in solution (the carbonic acid and CO_2 concentrations are relatively low under these conditions, see Section 2.3.1). Thus, $c(\mathrm{C_{tot}})$ can be approximated as shown in Eq. (2.10)

$$c(\mathrm{C_{tot}}) \approx c(\mathrm{HCO_3^-})+c(\mathrm{CO_3^{2-}}) \tag{2.10}$$

We can write via the Henderson-Hasselbalch equation (18)

$$\mathrm{pH} = \mathrm{p}K_{\mathrm{a2}} + \log\left(\frac{a(\mathrm{CO_3^{2-}})}{a(\mathrm{HCO_3^-})}\right) = \mathrm{p}K_{\mathrm{a2}} + \log\left(\frac{c(\mathrm{CO_3^{2-}})}{c(\mathrm{HCO_3^-})}\frac{\gamma(\mathrm{CO_3^{2-}})}{\gamma(\mathrm{HCO_3^-})}\right) \tag{2.11}$$

where the activity ratio $a(\mathrm{CO_3^{2-}})$ / $a(\mathrm{HCO_3^-})$ can be calculated as ~0.263. Using Eqs. (2.10) and (2.11), we can express the concentrations $c(\mathrm{HCO_3^-})$ and $c(\mathrm{CO_3^{2-}})$ as

$$c(\mathrm{HCO_3^-}) \approx \frac{c(\mathrm{C_{tot}})}{1+\left(\frac{a(\mathrm{CO_3^{2-}})}{a(\mathrm{HCO_3^-})}\frac{\gamma(\mathrm{HCO_3^-})}{\gamma(\mathrm{CO_3^{2-}})}\right)} \tag{2.12}$$

$$c(\mathrm{CO_3^{2-}}) \approx c(\mathrm{C_{tot}}) - \frac{c(\mathrm{C_{tot}})}{1+\left(\frac{a(\mathrm{CO_3^{2-}})}{a(\mathrm{HCO_3^-})}\frac{\gamma(\mathrm{HCO_3^-})}{\gamma(\mathrm{CO_3^{2-}})}\right)} \tag{2.13}$$

Since we take into account the activities of individual ions, we take $\gamma(\mathrm{CO_3^{2-}}) = \gamma(\mathrm{Ca^{2+}})$. Therefore, the only unknown parameters in Eq. (2.3) are $\gamma(\mathrm{HCO_3^-})$ and $\gamma(\mathrm{Ca^{2+}})$ which in turn can be determined using the Davies equation (19)

$$-\log \gamma(\mathrm{HCO_3^-}) = 0.50\left(\frac{I^{0.5}}{1+I^{0.5}} - 0.3I\right) \tag{2.14}$$

$$-\log \gamma\left(\mathrm{Ca^{2+}}\right) = 0.50\ z(\mathrm{Ca^{2+}})^2\left(\frac{I^{0.5}}{1+I^{0.5}} - 0.3I\right) \tag{2.15}$$

Using an iterative process, we found that at our determined ionic strength of I = 15.5 mM, on average $\gamma(\mathrm{Ca^{2+}}) = \gamma(\mathrm{CO_3^{2-}}) = 0.64 \pm 0.03$, and $\gamma(\mathrm{HCO_3^-}) = 0.87 \pm 0.03$ (where uncertainties represent one standard deviation of the distribution). These values are in good agreement with experimental values of activities of individual ions determined under similar conditions in the same setup by measuring diffusion potentials in 13 mM NaCl (a total ionic strength adjustment buffer (TISAB) solution), where $\gamma(\mathrm{Ca^{2+}}) = 0.69 \pm 0.02$ (see Kellermeier *et al.* (15)). Additionally, comparing our determined activity coefficients via the Davies equation (19) with the extended Debye-Hückel limiting law (20), we only find a discrepancy of 0.01 (i.e. $\gamma(\mathrm{Ca^{2+}}) = 0.64$ vs. 0.65 respectively), thus reliably letting us use this ionic strength model to determine $\gamma(\mathrm{Ca^{2+}})$. Moreover, we determined $c(\mathrm{HCO_3^-})$ = 7.24 mM and $c(\mathrm{CO_3^{2-}})$ = 2.76 mM.

An additional increase in ionic strength may be expected from the slow release of the 3 M KCl electrode reference solution via the diaphragm of the micro pH glass electrode into the sample solution. According to the manufacturer, at 25 °C, this release rate can range from 3 – 25 µL/h (21). At the highest flow rate, the change in ionic strength would be 3.13 mM, in which case $\gamma(\mathrm{Ca^{2+}})$ would drop to a value of 0.58, slightly below the standard deviation of the measurements. However, this is the upper limit, and release rates at 20 °C are expected to be lower. Additionally, Kellermeier *et al.* determined with addition of (high) concentrations of 0-120 mM NaCl to the ~10mM TISAB solution, that under these similar conditions the ionic strength remains virtually constant in the prenucleation stage (15).

2.2.4 Accuracy of pH measurement

pH errors may occur by 1) potential errors of the glass electrode-reference electrode pair 2) liquid junction potentials between the reference electrode and the sample solution and 3) by interfering ions such as $\mathrm{Na^+}$ and $\mathrm{Ca^{2+}}$ other than $\mathrm{H^+}$ at the glass membrane (also referred to as the alkaline error) (22).

According to Plummer *et al.* (23), liquid junction potentials determined via the Henderson equation (24) in the pH of Ca-$\mathrm{HCO_3}$ solutions at 25 °C for 4 M KCl reference electrolyte solutions only vary by a maximum of 0.03 pH at very low $\mathrm{Ca^{2+}}$ concentrations of approx. 0.1 mM. Kellermeier *et al.* showed that at pH 9.75 junction potentials are similar for the buffer and for the TISAB solution (approx. -2.5 mV with ≤ 8%

deviation) (15). Na^+ ions can replace—partially or completely—the hydrogen ions in the outer gel layer of the glass membrane, and thereby contribute to potential errors at the outer phase boundary of the electrode. According to the manufacturer, the alkali error should be prominent above ~pH 11 at high ionic strengths with concentrations of 1.0 M Na^+ or higher and thus this should be negligible in our experiments (16). Thus, this indicates that the presence of Ca^{2+} ions and Na^+ ions in our experiments do not affect pH measurements significantly.

2.3 Analysis of Ca^{2+} binding and NaOH addition

The bound fraction of the Ca^{2+} decreased slightly over time (Fig. S3), which is due to the slight increase in ionic strength as a result of (i) the continuous addition of $CaCl_2$ to the carbonate buffer (10 µL min^{-1}), and (ii) CO_2 influx, which despite the use of a N_2 atmosphere could not be fully prevented. The latter led to an increased concentration of H^+, which was directly titrated out by NaOH addition (see Fig. S4), and increased concentrations of HCO_3^- and CO_3^{2-}. Therefore, over time, the small increase in ionic strength resulted in a small decrease in the activity coefficient for calcium. As the standard error in NaOH addition is rather large compared to the standard error in the determined $c(Ca^{2+}_{bound})$, the amount of NaOH required to neutralize the H^+ released due to the formation of any prenucleation species cannot be adequately used to quantify the composition of such species (for more details, see Section S2.3.1- 2.3.3).

2.3.1 Activity of (bi)carbonate species in the system after influx of CO_2

In water, the hydration equilibrium constant K_H determines how much of the CO_2 is converted into H_2CO_3

$$K_H = \frac{c(H_2CO_3)}{c(CO_{2(aq)})} \tag{2.16}$$

Literature values of this parameter range between 1.1–2.6 × 10^{-3} at 25 °C (25), implying that CO_2 dominates the associated equilibrium, which greatly limits any effect on pH. To calculate $c(CO_{2(aq)})$ we use Henry's law,

$$p_{CO_2} = k_H \cdot c(CO_{2(aq)}) \tag{2.17}$$

with k_H representing Henry's law constant for solubility in water (29.41 L atm mol^{-1} at 25 °C (26)) and p_{CO_2} is the partial pressure of CO_2. With a CO_2 content in air of 0.0314 vol% (17), we get $p_{CO_2} = 3.14 \times 10^{-4}$ atm, which results in $c(CO_{2(aq)}) = 1.07 \times 10^{-5}$ M. Using Eq. (2.16) with K_H varying from 1.1 - 2.6 × 10^{-3} yields $c(H_2CO_3) = 1.2 - 2.8 \times 10^{-8}$ M.

To calculate the activity of carbonate species in solution, we use the apparent constant K_{app} (25)

$$K_{\mathrm{app}} = \frac{a(\mathrm{H^+})\cdot a(\mathrm{HCO_3^-})}{a(\mathrm{H_2CO_3})^{\#}} \tag{2.18}$$

with $\mathrm{p}K_{\mathrm{app}} = 6.35$ (17) and

$$c(\mathrm{H_2CO_3})^{\#} = c(\mathrm{H_2CO_3}) + c(\mathrm{CO_{2(aq)}}) \approx c(\mathrm{CO_{2(aq)}}) \tag{2.19}$$

We obtain $c(\mathrm{H_2CO_3})^{\#} \approx 1.07 \times 10^{-5}$ M. The equilibrium for carbonic acid/bicarbonate can now be expressed as

$$\mathrm{H_2CO_3} \rightleftarrows \mathrm{HCO_3^-} + \mathrm{H^+} \tag{2.20}$$

with $\mathrm{p}K_{\mathrm{a}} = 3.45 \pm 0.15$ (27) and

$$\mathrm{HCO_3^-} \rightleftarrows \mathrm{CO_3^{2-}} + \mathrm{H^+} \tag{2.21}$$

where $\mathrm{p}K_{\mathrm{a2}} = 10.33$ (17). Via the Henderson-Hasselbalch equation, this gives

$$\mathrm{pH} = \mathrm{p}K_{\mathrm{app}} + \log \frac{a(\mathrm{HCO_3^-})}{a(\mathrm{H_2CO_3})^{\#}} \tag{2.22}$$

$$\mathrm{pH} = \mathrm{p}K_{\mathrm{a2}} + \log \frac{a(\mathrm{CO_3^{2-}})}{a(\mathrm{HCO_3^-})} \tag{2.23}$$

with pH = 9.75, $\mathrm{p}K_{\mathrm{app}} = 6.35$, and $a(\mathrm{H_2CO_3})^{\#} = 1.07 \times 10^{-5}$, Eq. (2.22) gives $a(\mathrm{HCO_3^-}) = 2.7 \times 10^{-2}$. From this (and using $\mathrm{p}K_{\mathrm{a2}} = 10.33$), Eq. (2.23) gives $a(\mathrm{CO_3^{2-}}) = 7.1 \times 10^{-3}$.

2.3.2 Release of $\mathrm{H^+}$ by (bi)carbonate species generated due to $\mathrm{CO_2}$ influx

Eq. (2.20) and (2.21) show that when $\mathrm{CO_2}$ diffuses into the solution (and $\mathrm{H_2CO_3}$ is generated), bicarbonate and carbonate species are formed. This results in the subsequent release of protons: one or two protons are released during the conversion of $\mathrm{CO_2}$ into $\mathrm{HCO_3^-}$ or $\mathrm{CO_3^{2-}}$, respectively. On average, there is a release of 1.31 $\mathrm{H^+}$ per $\mathrm{CO_2}$ molecule. At the end of the reaction we added ~1 × 10^{-5} mol NaOH (N = 3 experiments) in ~25 mL due to diffusion of $\mathrm{CO_2}$ into the solution (and thus $\mathrm{H^+}$ generation). From this, the amount of $\mathrm{HCO_3^-}$/$\mathrm{CO_3^{2-}}$ generated was determined: $1 \times 10^{-5}/1.31 = 7.63 \times 10^{-6}$ mol. In a starting volume of 25 mL, we found a total concentration increase in $\mathrm{HCO_3^-}/\mathrm{CO_3^{2-}}$ of 0.3 mM. As the total concentration of carbonate in the solution (~10 mM) is larger than this smaller increase in carbonate concentration, this aspect of $\mathrm{CO_2}$ influx on the alteration of the ionic strength is therefore neglected (see also Section 2.3.3).

2.3.3 Binding behavior of Ca^{2+} with CO_3^{2-} or HCO_3^- in ion pairs

At a constant pH of 9.75 and temperature of 20 ± 1 °C, the ratio $c(HCO_3^{2-})/c(CO_3^{2-})$ is constant and in the 10 mM carbonate buffer $c(HCO_3^-)$ is stable at 7.24 mM. If calcium forms complexes with a carbonate ion in a 1:1 fashion ($CaCO_3^0$), the equilibrium shifts to replenish the amount of carbonate, eventually giving rise to a similar solution equilibrium. With this replenishing action, 0.724 mmol H^+ is released when 1 calcium binds to 1 carbonate (see Scheme S2).

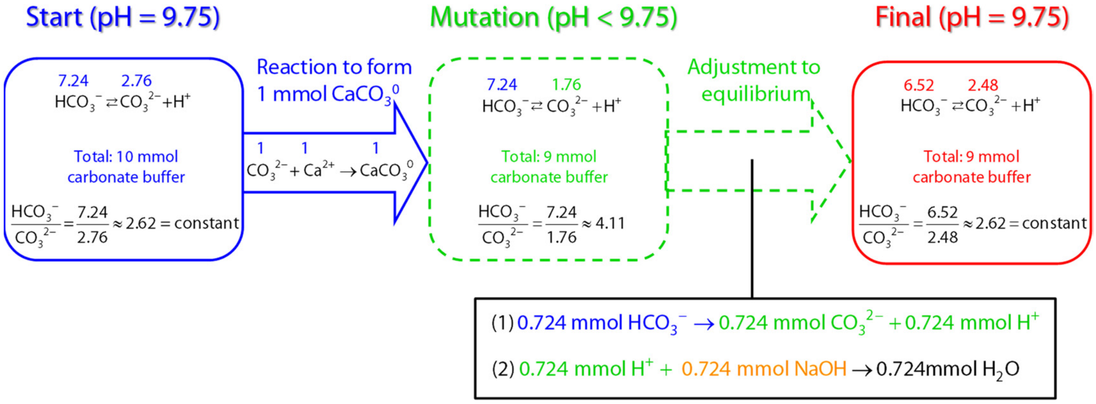

Scheme S2. Schematic representation of the adjustment of constant equilibrium between carbonate and bicarbonate at the used conditions in 1 L solution, when a complex of Ca^{2+}:CO_3^{2-} 1:1 ($CaCO_3^0$) is formed. The reaction leads to a total release of 0.724 mmol H^+ (adjustment to equilibrium (1)), which is compensated by titrating in the same amount of NaOH to yield a constant pH value (adjustment to equilibrium (2)).

If calcium forms complexes with a bicarbonate ion in a 1:1 fashion ($CaHCO_3^+$), the equilibrium shifts to replenish the amount of bicarbonate: 0.276 mmol H^+ is consumed when 1 calcium binds to 1 bicarbonate (see Scheme S3). In other words, formation of ion pairs with Ca^{2+}:CO_3^{2-} 1:1 would lead to a molar ratio of $NaOH/Ca^{2+}_{bound}$ = 0.724 (line 1, Fig. S2). On the other hand, ion pair formation of Ca^{2+}:HCO_3^- 1:1 in the prenucleation stage would lead to a consumption of 0.276 mmol H^+ per mmol Ca^{2+}_{bound} and 0.276 mmol H^+ per mmol Ca^{2+}_{bound} should be added to keep the pH constant. Thus, we have a molar ratio of $NaOH/Ca^{2+}_{bound}$ = –0.276 (line 2, Fig. S2). Two typical experimentally obtained NaOH curves after correction for H^+ release due to CO_2 influx are shown in Fig. S2 (line 3 and 4). The large spread between both curves (see also Fig. S4) demonstrates that the amount of NaOH addition is not sufficiently accurate to quantitatively determine a specific ion pair/cluster composition for these experiments. This is in contradiction with findings of Gebauer *et al.* (1), who quantitatively determined carbonate binding in prenucleation clusters based on titration with NaOH.

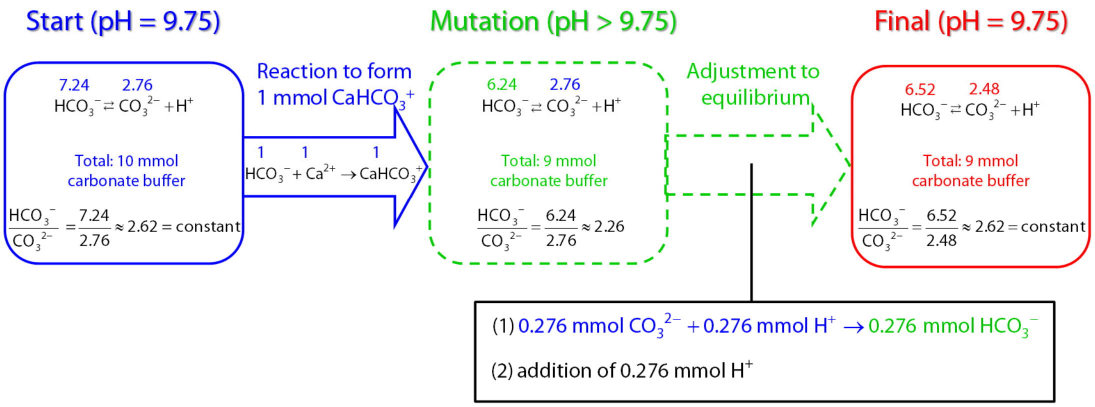

Scheme S3. Schematic representation of the adjustment of constant equilibrium between carbonate and bicarbonate at the used conditions in 1 L solution, when a complex of Ca^{2+}:HCO_3^- 1:1 ($CaHCO_3^+$) is formed. The reaction leads to a total consumption of 0.276 mmol H^+ in solution (adjustment to equilibrium (1)), which would be compensated by titrating in the same amount of acid to yield a constant pH-value (adjustment to equilibrium (2)).

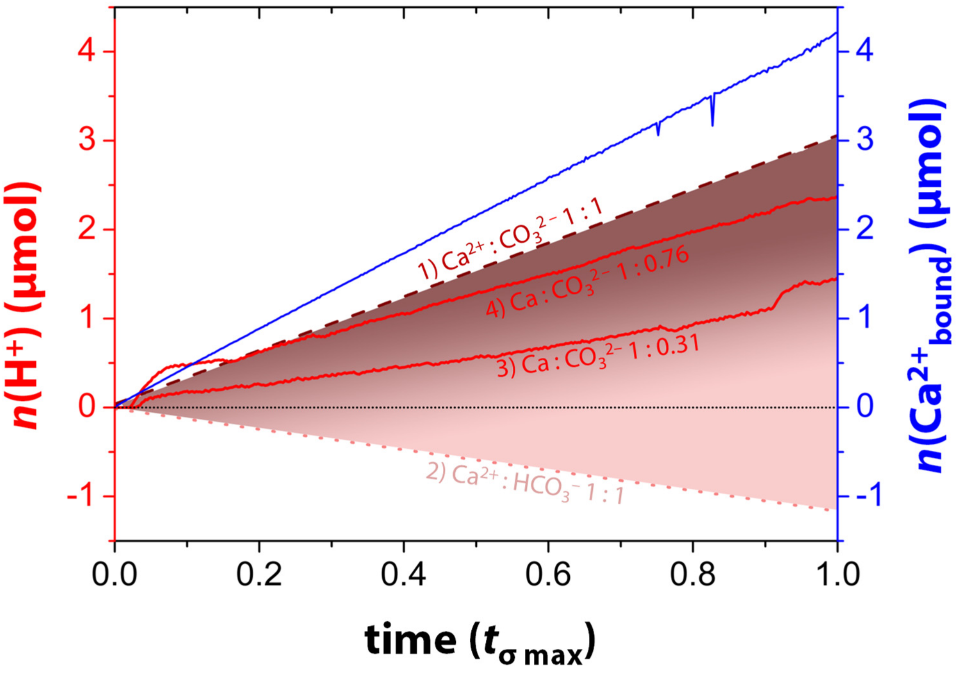

Figure S2. Binding of Ca^{2+} in ion pairs and corresponding change of H^+ as function of time in the prenucleation stage. The solid blue curve represents the $Ca^{2+}{}_{bound}$ (right y-axis). The left y-axis shows the amount of H^+ released (or amount of NaOH added) due to ion pair formation: Ca^{2+}:CO_3^{2-} 1:1 would lead to **1)** a H^+ release line with slope 0.724 with respect to the Ca^{2+}bound curve (dark red dashed line); Ca^{2+}:HCO_3^- 1:1 would lead to **2)** a H^+ release line with slope –0.276 with respect to the Ca^{2+}bound curve (light red dotted line). The color gradient in between 1) and 2) indicates the carbonate/bicarbonate presence in the prenucleation species: going more towards the darker red area predicts the presence of species with a higher carbonate content, while at lighter red the bicarbonate content would be higher. **3)** and **4)** are two examples of experimental H^+ release curves after CO_2 correction.

2.3.4 Equilibrium expressions for Ca^{2+} binding in ion pairs: 1 Ca^{2+} per ion pair

During the titration experiments, the ionic strength remains virtually constant (see also Kellermeier *et al.*(15)) and therefore activity coefficients are also approximately constant. Combining this information into the equilibrium constant K_{eq}, we are able to express the equilibrium of any calcium (bi)carbonate species. Here we provide a theoretical analysis for complexes $\text{Ca}_x^{2+}(\text{CO}_3^{2-})_y\text{H}_z^+$ – which we denote here as $A_xB_yC_z$ – having different x, y and z values, *i.e.* for any mixture of calcium-containing carbonate and bicarbonate complexes. We have equilibria of the form given below, where $x \geq 1$, $y \geq 1$ and $z \geq 0$ are integers.

$$x_i\text{A}+y_i\text{B}+z_i\text{C} \rightleftharpoons \text{A}_{x_i}\text{B}_{y_i}\text{C}_{z_i} \qquad K'_{\text{eq}}=\frac{\left(\text{A}_{x_i}\text{B}_{y_i}\text{C}_{z_i}\right)}{(\text{A})^{x_i}(\text{B})^{y_i}(\text{C})^{z_i}} \tag{2.24}$$

Since (B) and (C) are virtually constant, it is convenient to define an associated equilibrium constant K'^{*}_{eq}

$$K'^{*}_{\text{eq}}=\frac{K'_{\text{eq}}}{(\text{B})^{y_i}(\text{C})^{z_i}}=\frac{\left(\text{A}_{x_i}\text{B}_{y_i}\text{C}_{z_i}\right)}{(\text{A})^{x_i}} \tag{2.25}$$

The sum of bound calcium ions becomes

$$\left[\sum \text{bound Ca}\right]=\sum_i x_i\left[\text{A}_{x_i}\text{B}_{y_i}\text{C}_{z_i}\right]=\sum_i x_i\, K'^{*}_{\text{eq}}\, [\text{A}]^{x_i}=\sum_i x_i\, K'^{*}_{\text{eq}}\, (\text{A})^{x_i}\, \gamma^{-x_i} \tag{2.26}$$

Where γ is the activity coefficient. From this equation, the theoretically expected ratio between bound calcium and the activity of free calcium can be evaluated as

$$\frac{[\sum \text{bound Ca}]}{(\text{A})}=\sum_{\text{i}} x_i\, \text{K}'^{*}_{\text{eq}}\, (\text{A})^{x_i-1}\, \gamma^{-x_i} \tag{2.27}$$

The right-hand side of the equation demonstrates that only when all exponents (x_i –1) are zero, then the right-hand side is independent of (A). The left-hand side of Eq. (2.27) [∑ bound Ca]/(A) is given as the y-axis label of our experimentally determined Fig. S3. Thus, Fig. S3 demonstrates that $x = 1$ irrespective of the number of complex types.

Accordingly, we can express for the equilibrium of calcium carbonate species $\text{Ca}_x(\text{CO}_3)_y^{2(x-y)}$ in solution

$$K_{\mathrm{eq}\ 1}' = \frac{a(\mathrm{Ca}_x(\mathrm{CO}_3)_y^{2(x-y)})}{a(\mathrm{Ca}^{2+}{}_{\mathrm{free}})^x \cdot a(\mathrm{CO}_3^{2-}{}_{\mathrm{free}})^y} \tag{2.28}$$

Considering the high excess of carbonate in solution with respect to the added Ca^{2+}-ions—particularly in the early stages—the activity of carbonate species $a(\mathrm{CO}_3{}^{2-}{}_{\mathrm{free}})$ may be considered to be constant, reducing Eq. (2.28) to

$$\frac{a(\mathrm{Ca}_x(\mathrm{CO}_3)_y^{2(x-y)})}{a(\mathrm{Ca}^{2+}{}_{\mathrm{free}})^x} = \mathrm{constant} \tag{2.29}$$

Here, the bound calcium carbonate species have an activity coefficient of unity, thus $a(\mathrm{Ca}_x(\mathrm{CO}_3)_y{}^{2(x-y)}) = c(\mathrm{Ca}_x(\mathrm{CO}_3)_y{}^{2(x-y)})$. Likewise, an expression can be made for the equilibrium constant between free Ca^{2+} and complexes of Ca^{2+} and bicarbonate.

$$K_{\mathrm{eq}\ 2}' = \frac{c(\mathrm{Ca}_x(\mathrm{HCO}_3)_y^{2x-y})}{a(\mathrm{Ca}^{2+}{}_{\mathrm{free}})^x} \tag{2.30}$$

Based on the constant activity ratio of bound and free Ca^{2+} in the prenucleation stage as demonstrated in Fig. S3, from both Eq. (2.29) and Eq. (2.30) it automatically follows that $x = 1$ and that the behavior in the titration curve corresponds to an equilibrium calcium carbonate/bicarbonate complex with only 1 Ca^{2+} incorporated. This indicates that before nucleation occurs the majority of the prenucleation species are single Ca^{2+}-based ion association complexes, such as the classical ion pairs for calcium carbonate: $\mathrm{CaCO}_3{}^0$ and $\mathrm{CaHCO}_3{}^+$.

2.4 Fitting Titration Data to a Speciation Model

We used Visual MINTEQ (28) equilibrium speciation models to calculate the composition of inorganic ions and complexes (ion pairs) in water during the titration experiment. Knowing all the concentrations of every species at every time point, we inserted these at specific time-points along the titration curve (t = 0, 0.2, 0.4, 0.6, 0.8 and 1.0 $t_{\sigma\ \max}$) into MINTEQ, along with the fixed pH and temperature from our experimental set-up.

Values for equilibrium constants are determined by the program, which describes a polynomial for both $\mathrm{CaCO}_3{}^0$ and $\mathrm{CaHCO}_3{}^+$ ion pairs, which are given as

$$\log K_{\mathrm{CaCO}_3^0} = -1228.732 - 0.299444T + \frac{35512.75}{T} + 485.818 \log T \tag{2.31}$$

$$\log \mathrm{K}_{\mathrm{CaHCO}_3^+} = 1209.120 + 0.31294T - \frac{34765.05}{T} - 478.782 \log T \tag{2.32}$$

with T being the absolute temperature (23). MINTEQ is thus able to determine concentrations (and activities) of $CaCO_3^0$ and $CaHCO_3^+$ ion pairs. Since we add Ca^{2+} to the carbonate buffer, we would like to know how much of this material is bound in $CaCO_3^0$ and $CaHCO_3^+$ ion pairs, while the remainder would be considered free in solution as Ca^{2+} ions (Ca^{2+}_{total} = Ca^{2+}_{bound} + Ca^{2+}_{free}). We have used the standard thermodynamic database (thermos.vdb), and for the activity model, we employed the Davies equation that is integrated in the software as

$$-\log \gamma_{\mathrm{i}} = A\cdot z_i^2\left(\frac{\sqrt{I}}{1+\sqrt{I}} - B\cdot I\right) \tag{2.33}$$

Here, the Davies parameter B has a default value of 0.3, and A is the Debye-Hückel coefficient which is temperature dependent, and determined at the input temperature of 20 ˚C from the relationships given by Truesdell and Jones (29). Since CO_2 influx is directly compensated with NaOH titration and only leads to an increase of CO_3^{2-}/HCO_3^- of ~0.3 mM (i.e. 3%), we did not incorporate a partial pressure of CO_2 in our system. Neither did we suppress mineral formation at supersaturated conditions, since the first visual evidence of mineral in the form of vaterite is presented at 1.06 $t_{\sigma\,\max}$ (see Fig. 8d main text). A sample input file is shown below:

pH:	Fixed at 9.75	
Temperature:	20˚C	
Ionic strength:	15.5 mM	
Concentrations:	$[H^+]$	1.778E-7 mM
	$[Ca^{2+}]$	0.052 mM
	$[Na^+]$	12.528 mM
	$[Cl^-]$	0.105 mM
	$[CO_3^{2-}]$	2.76 mM
List of fixed species:	log $a(H^+)$ = -9.75	
	log $a(HCO_3^-)$ = -2.180	

As a result, MINTEQ determines comparable amounts of Ca^{2+}_{bound} (only in ion pairs in a 96:4 $CaCO_3^0$:$CaHCO_3^+$ ratio), and free Ca^{2+} as in the titration experiments. This suggests that the Ca^{2+}-titration profiles can be explained by ion pair formation and thus not, per se, by involvement of prenucleation clusters.

Table S4. Distribution of concentrations and activities of ions and ion pairs as determined by MINTEQ. The total amount of bound Ca^{2+} (blue) is >99% of all dosed Ca^{2+}, in $CaCO_3^0$ (~96%) and $CaHCO_3^+$ (~4%) ion pairs. Similarly, >99% of Na^+ (green) is bound in $NaCO_3^-$ (~91%) and $NaHCO_3$ (~9%) ion pairs.

Species name	**0.20 $t_{\sigma\,max}$**			**0.40 $t_{\sigma\,max}$**			**0.80 $t_{\sigma\,max}$**			**$t_{\sigma\,max}$**		
	***c* (M)**	***a* (-)**	**% Ca^{2+}_{bound} Na^{+}_{bound}**	***c* (M)**	***a* (-)**	**% Ca^{2+}_{bound} Na^{+}_{bound}**	***c* (M)**	***a* (-)**	**% Ca^{2+}_{bound} Na^{+}_{bound}**	***c* (M)**	***a* (-)**	**% Ca^{2+}_{bound} Na^{+}_{bound}**
Ca^{2+}	2.09E-05	1.28E-05		4.18E-05	2.56E-05		8.29E-05	5.09E-05		1.03E-04	6.33E-05	
$CaCl^+$	3.27E-09	2.89E-09		1.29E-08	1.14E-08		5.02E-08	4.44E-08		7.70E-08	6.82E-08	
$CaCO_3$ (aq)	3.04E-05	3.05E-05	**96.4**	5.99E-05	6.01E-05	**96.4**	1.16E-04	1.16E-04	**96.4**	1.42E-04	1.42E-04	**96.4**
$CaHCO_3^+$	1.12E-06	9.90E-07	**3.6**	2.21E-06	1.95E-06	**3.6**	4.26E-06	3.77E-06	**3.5**	5.22E-06	4.62E-06	**3.5**
$CaOH^+$	1.05E-08	9.31E-09		2.10E-08	1.86E-08		4.18E-08	3.70E-08		5.19E-08	4.60E-08	
Cl^-	1.04E-04	9.23E-05		2.06E-04	1.83E-04		4.04E-04	3.57E-04		4.98E-04	4.41E-04	
CO_3^{2-}	2.55E-03	1.56E-03		2.52E-03	1.54E-03		2.44E-03	1.50E-03		2.40E-03	1.48E-03	
H^+	2.01E-10	1.78E-10		2.01E-10	1.78E-10		2.01E-10	1.78E-10		2.01E-10	1.78E-10	
H_2CO_3 (aq)	2.82E-06	2.83E-06		2.78E-06	2.79E-06		2.70E-06	2.71E-06		2.66E-06	2.67E-06	
HCO_3^-	7.46E-03	6.60E-03		7.36E-03	6.51E-03		7.15E-03	6.33E-03		7.04E-03	6.24E-03	
Na^+	1.21E-02	1.07E-02		1.20E-02	1.06E-02		1.19E-02	1.05E-02		1.18E-02	1.05E-02	
NaCl (aq)	5.21E-07	5.23E-07		1.02E-06	1.03E-06		1.98E-06	1.99E-06		2.43E-06	2.44E-06	
$NaCO_3^-$	4.05E-04	3.58E-04	**91.1**	3.97E-04	3.51E-04	**91.0**	3.81E-04	3.37E-04	**90.8**	3.73E-04	3.31E-04	**90.7**
$NaHCO_3$ (aq)	3.85E-05	3.86E-05	**8.7**	3.77E-05	3.78E-05	**8.7**	3.63E-05	3.64E-05	**8.6**	3.55E-05	3.57E-05	**8.6**
NaOH (aq)	5.03E-07	5.05E-07		5.00E-07	5.02E-07		4.95E-07	4.96E-07		4.92E-07	4.94E-07	
OH^-	4.36E-05	3.86E-05		4.36E-05	3.86E-05		4.36E-05	3.86E-05		4.35E-05	3.86E-05	

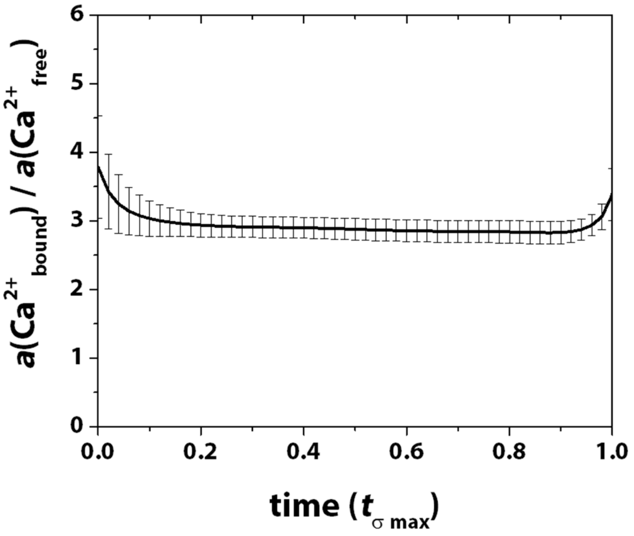

Figure S3. Activity ratio of bound to free Ca^{2+} ions in solution (with $a(Ca^{2+}_{bound}) = c(Ca^{2+}_{bound})$, see SI S2.3.4) up until $t_{\sigma\ max}$. Error bars are standard errors of the mean. Deviation of the constant ratio $\lesssim 0.1\ t_{\sigma\ max}$ is attributed to electrode signal instability during the calibration at very low ionic strength.

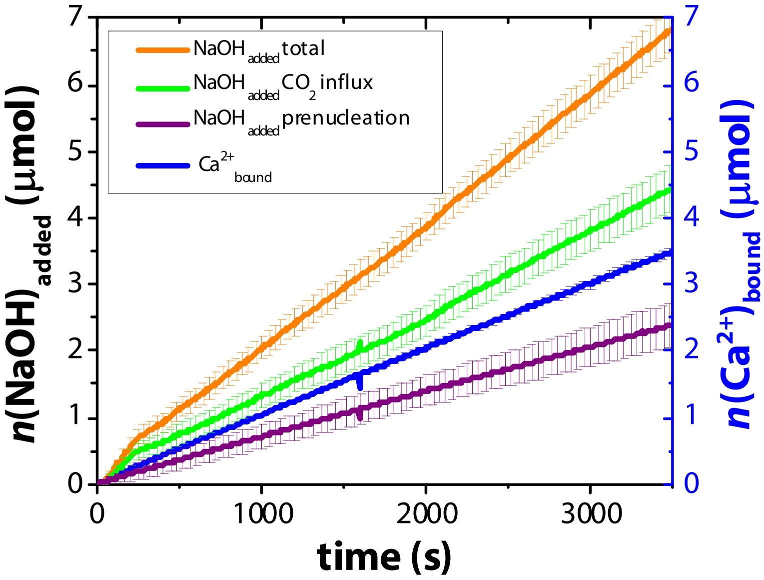

Figure S4. Added NaOH as a function of time (in seconds) in titration experiments. On the primary *y*-axis, the amount of added NaOH (in µmol) is given by the orange data points, which is composed for the largest part of H^+ influx due to CO_2-diffusion (green), measured by performing the same titration experiment without addition of $CaCl_2$ solution (reference; $N = 3$ experiments). Since there was no nucleation taking place in the latter experiment, we have compared slopes absolutely. The difference between the orange and green curve (purple curve) is the NaOH added to neutralize H^+ released due to Ca^{2+}-binding in prenucleation species. CO_2 influx correction was done to yield H^+ added due to calcium binding in prenucleation species. Bound calcium is given on the secondary *y*-axis (blue). All error bars are standard errors of the mean.

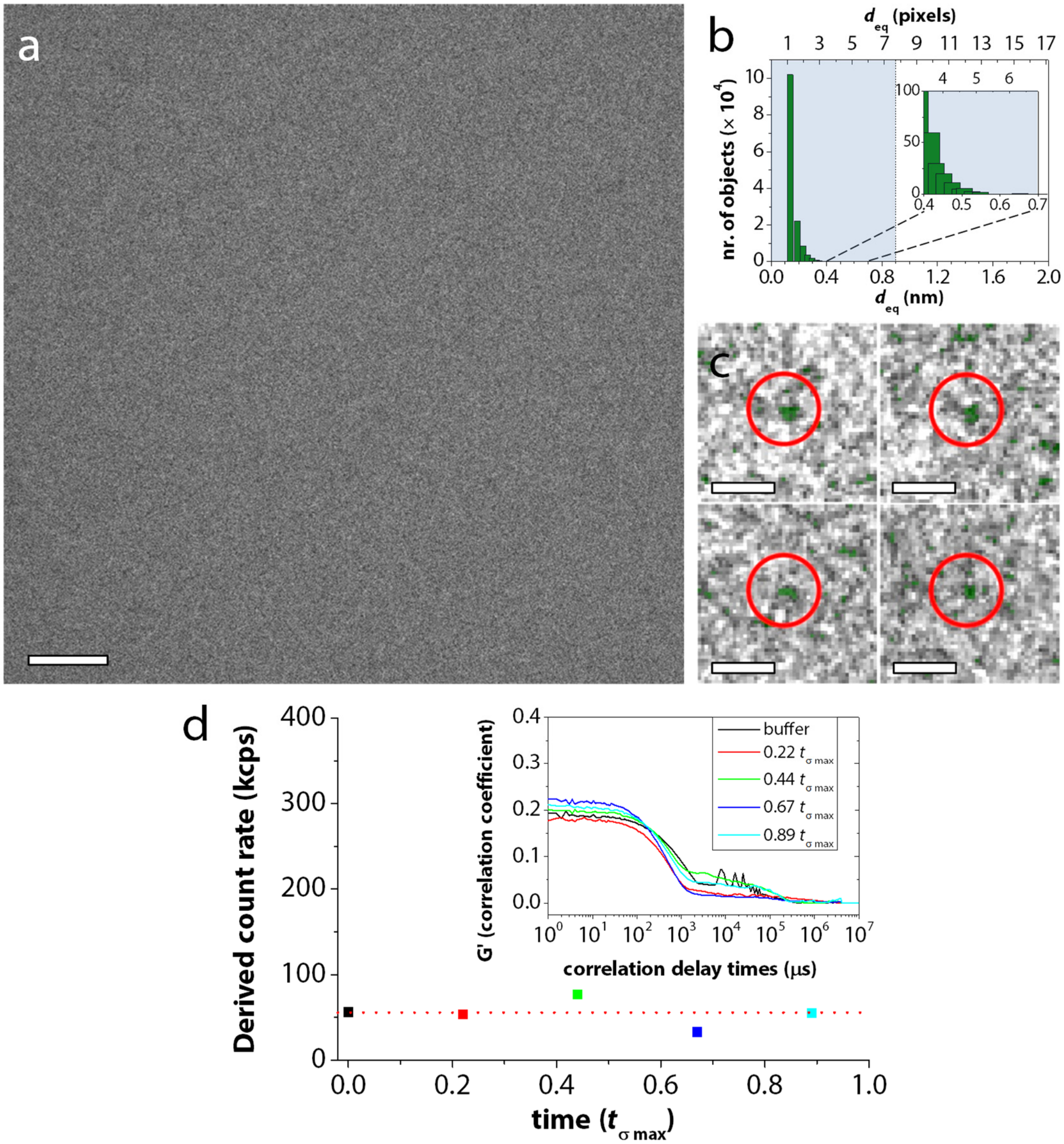

Figure S5. Investigation of prenucleation stage species with the use of cryo-TEM and DLS **(a)** A cryo-TEM image at 0.86 $t_{\sigma\ \max}$ (–0.5 µm defocus, scalebar: 20 nm) Pixel size = 0.12 nm. **(b)** The size distribution (number of objects vs. size) of the image in (a) was found utilizing the image analysis procedure (Materials and Methods 1.9). The primary *x*-axis shows the equivalent diameter d_{eq} of the objects in nm, while the secondary *x*-axis shows d_{eq} in pixels. The shaded blue area (d_{eq} = 0–0.9 nm; with the inset showing a zoom-in of the graph) indicates that all the objects in the image under the adopted imaging conditions are below the lowest interpretable resolution of 0.9 nm. Examples of these are found in **(c)**. The largest objects identified in (a) are highlighted in green (scale bar: 2 nm). No objects larger than 0.9 nm are observed. **(d)** DLS measurements in the prenucleation stage show insufficient scattering intensity for the existence of nanometer-sized prenucleation clusters. Typical derived count rate for 5 measurements, including that of the buffer. The average count rate is given by the red dotted line (<100 kcps). The inset shows the low correlation coefficient G' (≲ 0.7, i.e., a very low signal-to-noise-ratio) *vs*. correlation delay times for the same color-coded measurements.

2.5 Microscopic $CaCO_3$ Formation in Experiments

During the transition to the solid phase, calcium, as well as NaOH is consumed, indicated by an increase in amount of Ca^{2+}_{bound} and NaOH in solution, respectively (ΔCa^{2+}_{vat} and $\Delta NaOH_{vat}$). These can be quantified by following the procedure shown in Fig. S6 b. The constant slopes of n(NaOH) and $n(Ca^{2+}_{bound})$ in the prenucleation stage can be extrapolated to the bending point (BP; minimum in the derivative of the measured free Ca^{2+} line, see Fig. S1). Similarly, the constant slopes of n(NaOH) and $n(Ca^{2+}_{bound})$ in the postnucleation stage can be extrapolated to the BP, whereafter ΔCa^{2+}_{vat} and $\Delta NaOH_{vat}$ can be determined. Note that $\Delta NaOH_{vat}$ does not have to be corrected for CO_2 diffusion into the solution here, since the relative difference at the BP is similar.

The net transfer of ions towards the solid phase ($Ca^{2+}:CO_3^{2-} = 1:1$) would yield $\Delta Ca^{2+}_{vat}/\Delta NaOH_{vat} = 1.38$ (or 1/0.724 H^+ released per Ca^{2+}_{bound}), which fits within the experimental error.

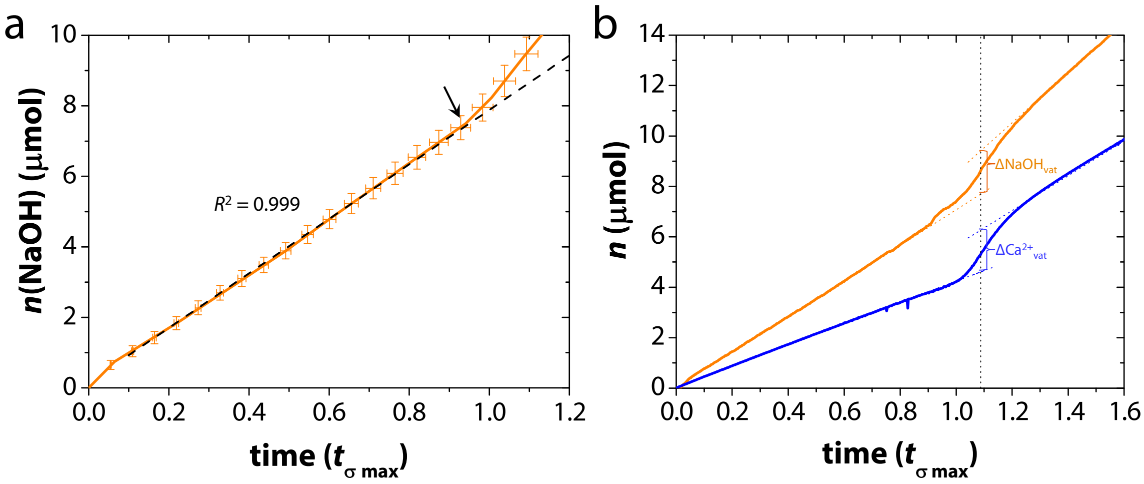

Figure S6. Onset of microscopic $CaCO_3$ formation and involvement of moles (n) of NaOH ($\Delta NaOH_{vat}$) and bound Ca^{2+} (ΔCa^{2+}_{vat}) during solid $CaCO_3$ formation. **(a)** Titration curve demonstrating the total amount of NaOH added (n(NaOH); orange) *vs*. normalized time $t_{\sigma\ max}$, averaged for $N = 10$ experiments with corresponding error bars (standard error). The black dotted line shows an extrapolated linear fit (R^2 is shown) from 0.1-0.9 $t_{\sigma\ max}$, to clearly indicate the onset of an increase in NaOH addition (black arrow). **(b)** Graph displaying the change in bound Ca^{2+} (ΔCa^{2+}_{vat}; blue continuous line) and NaOH ($\Delta NaOH_{vat}$; orange continuous line) consumed in the reaction as solid $CaCO_3$ precipitates in a typical titration experiment. Extrapolated dotted lines of the constant slopes in pre- and postnucleation stage for NaOH (orange) and Ca^{2+} bound (blue) are given towards the BP (black vertical line).

Table S5. **Data for $\Delta NaOH_{vat}$ (orange), ΔCa^{2+}_{vat} (blue), and $\Delta Ca^{2+}_{vat}/\Delta NaOH_{vat}$ (red) at the bending point, BP, for *N* = 10 experiments.**

Experiment nr.	BP ($t_{\sigma\ max}$)	$\Delta NaOH_{vat}$ (μmol)	ΔCa^{2+}_{vat} (μmol)	$\Delta Ca^{2+}_{vat}/\Delta NaOH_{vat}$
1	1.09	2.01	1.99	0.99
2	1.09	1.72	1.95	1.14
3	1.09	2.09	1.97	0.94
4	1.10	0.88	1.54	1.75
5	1.09	1.02	1.74	1.70
6	1.07	1.25	2.28	1.82
7	1.08	0.93	2.02	2.17
8	1.09	2.40	2.55	1.06
9	1.08	1.62	1.91	1.18
10	1.08	1.00	1.88	1.87

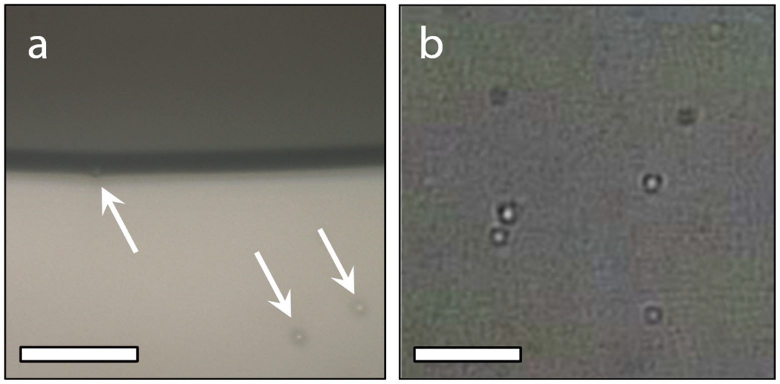

Figure S7. $CaCO_3$ formation as shown by optical microscopy. **(a)** Polarized optical microscopy (POM) image at 0.96 $t_{\sigma\ max}$ after drying of surrounding solution (dark) shows micrometer-sized entities which are indicated with white arrows that do not show birefringent behavior. **(b)** OM in reflection mode at 0.96 $t_{\sigma\ max}$ showing ~1.5–3 micrometer-sized entities. Scale bars are 20 μm.

Our polarized optical microscopy (POM) data cannot distinguish between the liquid or solid nature of the microscopic objects. Additionally, if indeed solid, it could be impossible to distinguish between the birefringence of an amorphous solid *vs*. a randomly oriented nanocrystalline structure (*e.g*. vaterite, see Section S2.6), since the resolution of POM to detect such nanocrystals is too low. Even though we do not directly observe carbonate bands of vaterite in FTIR at this stage (Fig. 8d main text), we do not entirely exclude the possibility that vaterite may be able to nucleate within the DLP, since this may be related to the small amount of nanocrystals present at this time.

2.6 Solid $CaCO_3$ – Vaterite

Fig. S8 a and b show SEM images taken at 1.03 $t_{\sigma\ \mathrm{max}}$ which indicate that vateritic structures appear, containing a rough corrugated spherical morphology. Fig. S8 c shows *in situ* ATR-FTIR measurements performed at $t > t_{\sigma\ \mathrm{max}}$ after the solubility of vaterite had been reached. Three subsequent measurements of a sample taken at 1.40 $t_{\sigma\ \mathrm{max}}$ indicate that the intensity in the carbonate stretches increased due to sedimentation of vaterite particles/aggregates.

In DLS, after $t_{\sigma\ \mathrm{max}}$ was reached, the correlation coefficient, *G*', decreased from its maximum value as indication of fluctuations in the number of large particles (Fig. S9 a). The small increases in *G*' at high correlation delay times from ~2 × 10^5 μs onwards indicate that this can be attributed to the formation of large μm-sized particles (and/or aggregates) that sediment, in line with FTIR observations in Fig. S8 c. Indeed, macroscopically the solution turned turbid after ~$t_{\sigma\ \mathrm{max}}$. Growth behavior at $t > t_{\sigma\ \mathrm{max}}$ of submicrometer- sized objects was confirmed by the shift to a larger particle size in the volume distribution (Fig. S9 b).

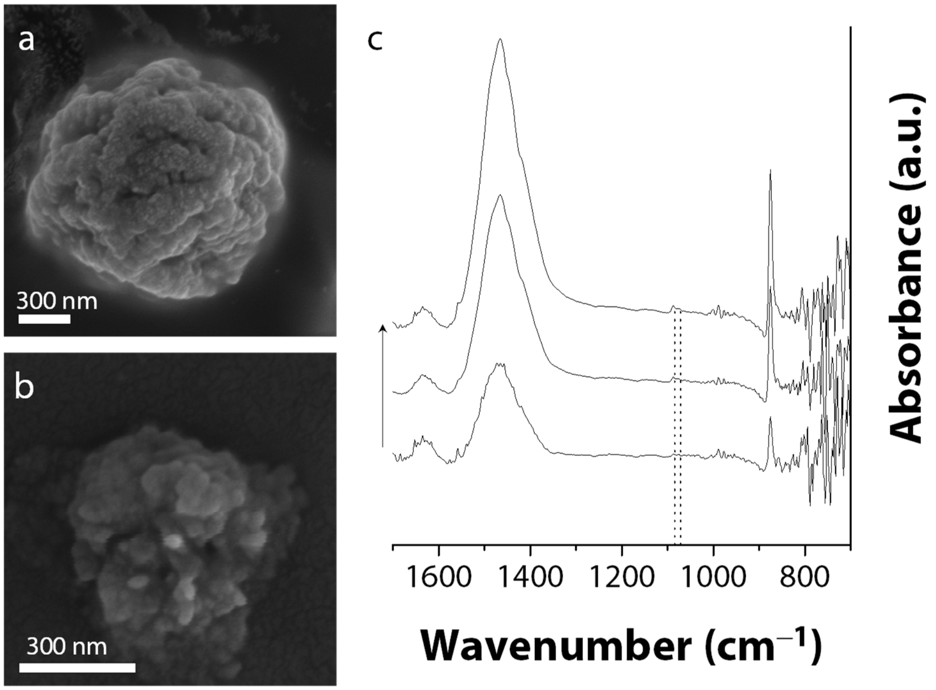

Figure S8. Vaterite formation as demonstrated by **(a,b)** SEM and **(c)** *in situ* ATR-FTIR. (a,b) SEM images at 1.03 $t_{\sigma\ \mathrm{max}}$. Scale bars are 300nm. (c) ATR-FTIR measurements of a sample taken at 1.40 $t_{\sigma\ \mathrm{max}}$. The evolution of the sample over time (indicated by the arrow) is marked by changes in the measured intensities for carbonate vibrational modes typical of vaterite at 875 cm^{-1} (CO_3^{2-} v_2 out of plane bend), 1087/1072 cm^{-1} (CO_3^{2-} v_1 symmetric stretch) and 1465 cm^{-1} (CO_3^{2-} v_3 asymmetric bond stretch).

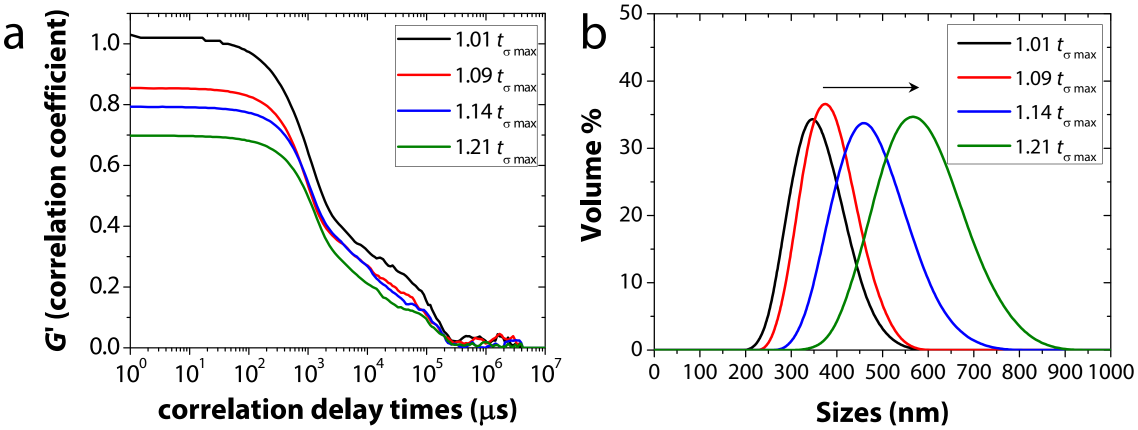

Figure S9. **(a)** The correlation diagrams of a typical experiment at 1.01, 1.09, 1.14 and 1.21 $t_{\sigma\ max}$. **(b)** Corresponding volume distributions from the deconvolution of the first decay in the correlation diagrams in (a), which indicate particle growth in the direction of the black arrow.

2.7 Experimental $CaCO_3$ Formation prior to Vaterite: DLP

2.7.1 Cryo-TEM Analysis of the DLP

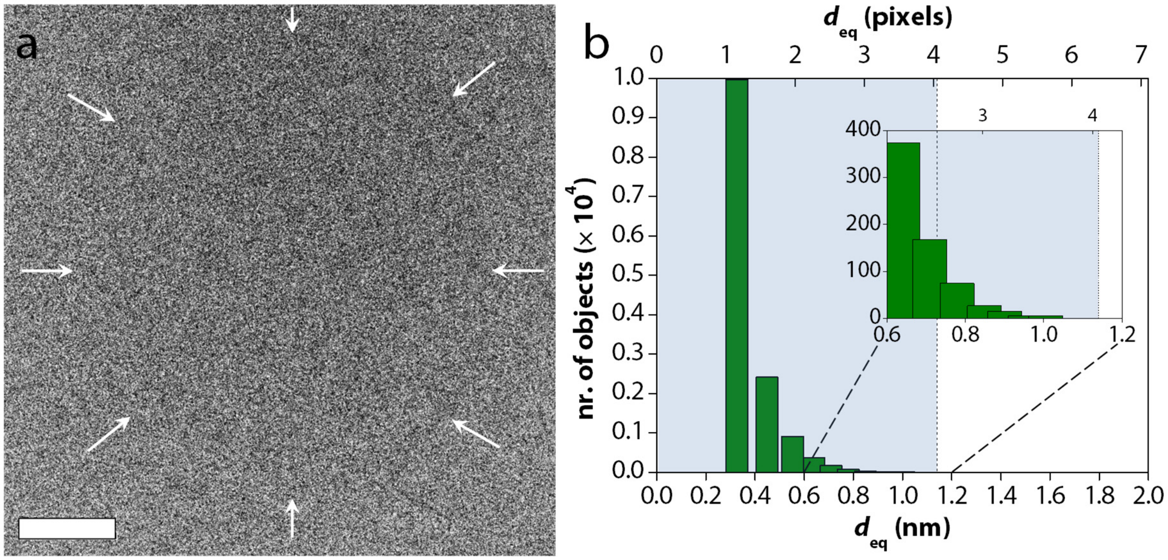

Figure S10. Absence of detected nanoparticles within and surrounding the DLP phase in cryo-TEM. (**a** shows a cryo-TEM image of a DLP particle at 0.96 $t_{\sigma\ max}$ (–0.5 μm nominal defocus, scale bar 50 nm); pixel size = 0.28 nm. The edge of the DLP is indicated by white arrows. **(b)** displays the equivalent diameter (d_{eq}) distribution of objects in the image in (a) using the image analysis procedure in Materials and Methods 1.9. The primary x-axis shows d_{eq} in nm, while the secondary x-axis shows d_{eq} in pixels. The shaded blue area (d_{eq} = 0 – 1.14 nm) indicates that all the objects in the image under the adopted imaging conditions are below the lowest interpretable resolution of 1.14 nm. The inset displays that the largest objects in the image are < 1 nm.

The electron diffraction patterns of the DLP, its background solution and pure water were radially integrated to produce a radial intensity profile (see Materials and Methods 1.9.2). The first ring of the diffraction pattern yielded a *d*-spacing which was probed for statistical differences following Pouget *et al.*(3) by the use of a Welch-Aspin generalized T-test, presented in Table S6.

Table S6. Welch-Aspin T-test results for the difference in *d*-spacing of water, background solution at 0.96 $t_{\sigma\ \mathrm{max}}$, and the DLP (sample 0.96 $t_{\sigma\ \mathrm{max}}$).

sample comparison	***T***	***P*-value (two-tailed)**
water - 0.96 $t_{\sigma\ \mathrm{max}}$	6.6575	0.0012
water - sample 0.96 $t_{\sigma\ \mathrm{max}}$	7.6056	0.0047
0.96 $t_{\sigma\ \mathrm{max}}$ - sample 0.96 $t_{\sigma\ \mathrm{max}}$	5.5688	0.0051

2.7.2 Phase separation and coarsening mechanism

Commonly, three characteristic regimes can be recognized during the spinodal decomposition (SD) process: (i) early, (ii) intermediate and (iii) late stage (30). Here, the early stage is often described by the Cahn-Hilliard-Cook theory (31, 32). The phase separation process is followed by coarsening processes which ultimately result in the formation of two or more distinct phases. These different stages often display particle growth kinetics that include multiple power-law regimes of the form t^{α} as observed by light scattering.

Coarsening can proceed via two possible mechanisms: either Ostwald ripening (also termed Lifshitz–Slyozov–Wagner (LSW) mechanism), or coalescence induced by Brownian collisions. The latter is also termed the Binder–Stauffer–Siggia (BSS) mechanism, after Siggia (33), and Binder and Stauffer (34). Wong *et al.* (35) found that for both Ostwald ripening and coalescence following nucleation a rate law $r \sim t^{1/3}$ can apply, and therefore we cannot distinguish between both such coarsening mechanisms. Following SD, the scaling exponent has been reported to be $\alpha = 1/3$ in the intermediate (or diffusive) and $\alpha \approx 1$ in the late (or flow) stage of the coarsening regime (33, 36, 37).

Both the onset of SD as well as the coarsening that follows phase-separation by nucleation have previously been described by power-law regimes with $\alpha = 1/3$ (35, 36). Given the fact that the $t^{1/3}$ power-law fits well to our DLS data over the whole regime from approximately $t_{\sigma\ \mathrm{max}}$ onwards, this indicates that SD or nucleation is nearly instantaneous, or that the coarsening and nucleation/SD regimes both follow the same power law. Higher order exponent coarsening regimes in late post-separation processes in SD of the form t^{α} with $\alpha \neq 1/3$ are not observed in our light scattering data. While this does not necessarily exclude SD as our observed phase separation mechanism, the fact that we are below the spinodal limit as determined in the work of Zou *et al.* (38) strongly suggests we obtain a liquid-liquid phase-separation though nucleation.

3. Simulation Data

3.1 Simulations at moderate supersaturation and basic pH

Previous computational investigations have identified the existence of Dynamically Ordered Liquid-Like Oxyanion Polymers (DOLLOPs) in solutions over a range of pH and concentrations (7). Three random solutions were prepared containing 14–47 cations and 22–64 anions, having solution concentrations of $c(\mathrm{C})$ = 30–50 mM and $c(\mathrm{Ca}^{2+})$ = 20–30 mM, and spanning a pH range from 9.9 to 10.3 (see Table S1 Materials and Methods). Furthermore, to validate that equilibrium had been achieved over this time, a $\mathrm{Ca_{14}(CO_3)_6(HCO_3)_{16}}$ cluster (Fig. S11) was immersed into water and allowed to relax.

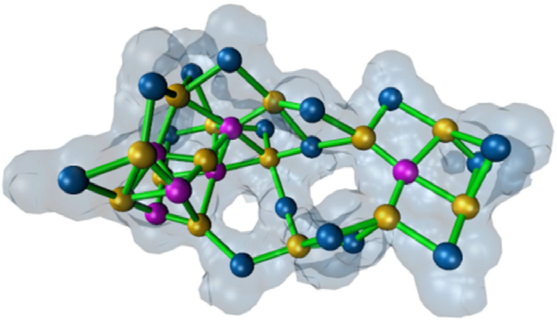

Figure S11. Initial configuration for a simulation of a neutral cluster containing 22 anions and 14 cations in water. Ca^{2+} and C atoms of $\mathrm{CO_3}^{2-}$ and $\mathrm{HCO_3}^{2-}$ are shown as yellow, purple and blue, respectively (O and H atoms are omitted for clarity). Green lines show distances between ions where $r \leq 4.2$ Å. The surface of the cluster, constructed as a van der Waals radius from atom centers and including O and H atoms is shown in grey. The average coordination number of calcium is 4 in this cluster.

Random and cluster systems equilibrated to the same state, producing a solution of free ions and small associates (Fig. S12). A large probability for ion-pairs was observed (where calcium to carbonate (Ca–C) coordination is defined as $r_{\mathrm{Ca–C}} \leq 4.2$ Å). Furthermore, binding affinities for calcium to carbonate or bicarbonate showed a preference for $\mathrm{CaCO_3}^0$ ion pairs in all simulations (Fig. S13). There was a small probability of finding ion trimers and a smaller probability still for the presence of two ion pairs bound in a single cluster. All cluster size distributions followed an exponential decay. Equilibrium concentrations and pH (see Table S1) were in the range $c(\mathrm{C})$ = 16–26 mM, $c(\mathrm{Ca}^{2+})$ = 3–5 mM and a pH of approximately 8.

Ion attachment and detachment frequencies to/from clusters was calculated as 0.018, 0.032 and 0.034 ps^{-1} for the three random simulations with $c(\mathrm{Ca}^{2+})$ = 19.6, 32.1 and 35.9 mM, respectively.

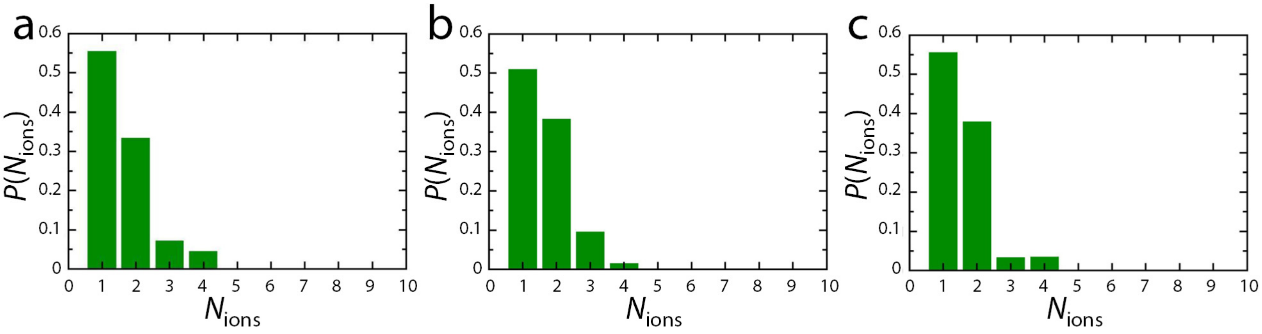

Figure S12. Cluster size probability distributions for ionic species containing N_{ions} ions measured during the final 2 ns of a 20 ns simulation. **(a)** and **(b)** are random systems simulated with 14 and 29 calcium ions, respectively. **(c)** shows size probabilities for a cluster system with composition equivalent to the ratio of ions in (a). The dominant peak for all clustered species (*i.e* for $N_{ions} > 1$) in systems at equilibrium is around $N_{ions} = 2$, and is due to the dominance of ion pairs. The data shows that both random and cluster systems at the same concentration (a and c) converge to the same equilibrium distribution of species by 10 ns of simulation, and that system size did not appear to affect the equilibrium state.

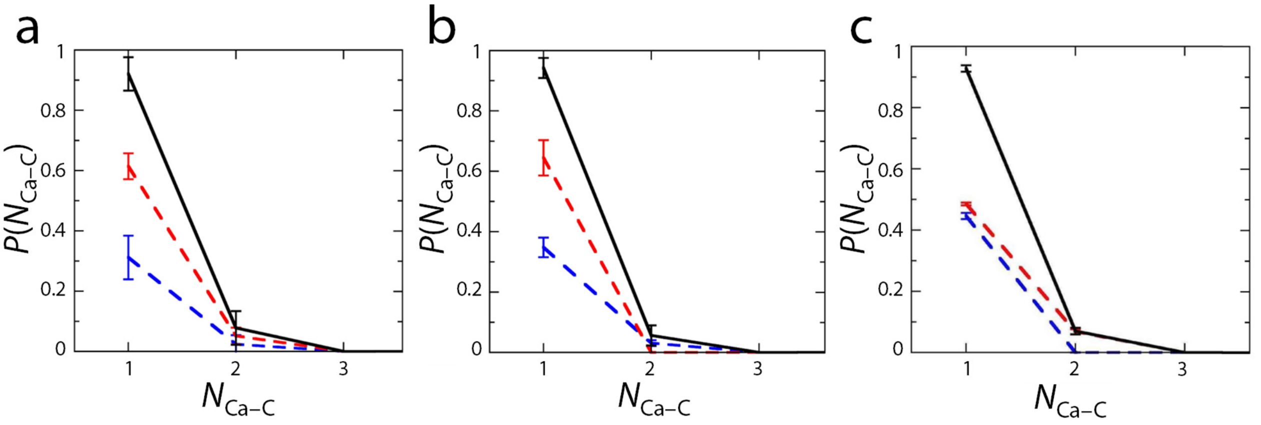

Figure S13. Probability of a Ca^{2+} ion coordinating to N_{Ca-C} carbon (black) atoms in associated species. Binding to carbon of carbonate (red) and bicarbonate (blue) is also shown. **(a)** and **(b)** are random systems simulated with 14 and 29 calcium ions respectively. **(c)** shows probabilities for a cluster system with composition equivalent to the ratio of ions in (a). Averages are measured from the final 5 ns of 15 ns trajectories and uncertainties of one standard deviation in the distribution are shown.

3.2 Simulations of Cluster Stability at 20–50 mM

In order to investigate the equilibrium between liquid-like clusters and small ion association complexes in solution, a series of simulations were performed at the limit of high pH, that is for systems lacking bicarbonate. CO_3^{2-} offers higher bond ordering than HCO_3^-, leading to larger, more stable clusters, and so simulations in the absence of HCO_3^- should overestimate the equilibrium cluster sizes. Furthermore, as the formation of DOLLOP is diffusion-limited, cluster systems were investigated as opposed to random ionic solutions.

A $Ca(CO_3)_{20}$ cluster with low density was simulated at 20 mM for 20 ns in water. Partial dissociation was observed with a small cluster $(CaCO_3)_2$ dissolving into solution; with the coordination distribution for Ca^{2+} to C approaching that reported for DOLLOP at high pH (7). The largest cluster contained 36 ions, for which a snapshot is provided in Fig. S14. Subsequently, bulk water was removed from the final configuration to produce systems with concentrations 20–50 mM, in ~10 mM increments. A short, 300 ps simulation was performed to relax water with ion coordinates frozen. This was taken to be $t = 0$, from which 27–60 ns simulations—with all atoms mobile—were performed (input parameters for which are provided in Materials and Methods 1.10). The coordination probabilities for calcium at $t = 0$ are provided in Fig. S14.

The mass-weighted average cluster size, S, decreases exponentially with time at all concentrations, with no evidence of an equilibrium being reached within the timescale of the simulations (Fig. S15 a). Dissolution rates are readily calculated as the slope of the semi-log plot, giving values of –0.100 ± 0.010, −0.032 ± 0.003, −0.056 ± 0.004 and −0.029 ± 0.004 ns^{-1}, for systems where $c(C)$ = 20, 30, 40 and 50 mM at $t = 0$, respectively. Average and maximum cluster sizes at the end of simulation are shown in Fig. S15 b. At 20 and 40 mM these values are, within statistical uncertainties, consistent with ion pairs. Larger clusters are seen at 30 and 50 mM, though we note that from the $\ln(S(t))$ plots that, for all examined concentrations, dissolution is still in progress at this stage, and so these are overestimates of the equilibrium cluster sizes. We conclude that the probability of finding large clusters under typical experimental conditions (10–50 mM) is very low.

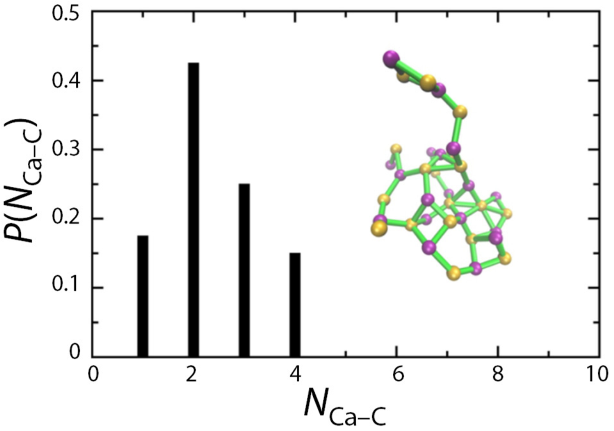

Figure S14. Probabilities for calcium to coordinate N_{Ca-C} carbon atoms in the initial cluster at the beginning of simulations at 20-50 mM. Inset is a snapshot of a neutral cluster containing 36 ions which was present in solution, where calcium and carbon are shown as yellow and purple, respectively (oxygen and hydrogen are omitted for clarity). Green lines show distances between ions where $r_{Ca-C} \leq 4.2$ Å.

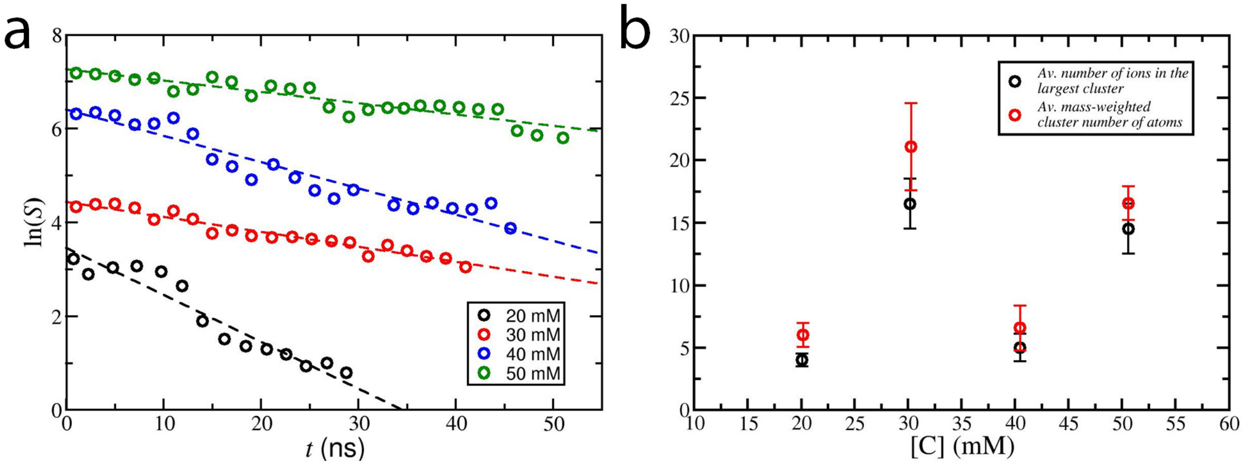

Figure S15. Spontaneous dissolution of clusters. **(a)** ln(S) as a function of time for systems with c(C) = 20–50 mM at t = 0. The data has been shifted for clarity as follows, ln(S)–1, ln(S), ln(S)+2, ln(S)+3 for c(C) = 20, 30, 40 and 50 mM, respectively. **(b)** The average cluster size in units of number of atoms, and average largest cluster size in units of number of ions at the end of the simulation for all concentrations studied for systems with 20 calcium and 20 carbonate ions. Error bars show uncertainties of one standard deviation in the data from the final 2 ns of simulation (as this time window was fixed, there may be some bias in the data for larger concentrations as cluster dissolution is slower).

The S(t) curves reveal a strong stochastic element to the dissolution process, as is seen most clearly at 20 mM (Fig. S16 a), where a sudden and rapid decrease of S occurs at 5–15 ns, superimposed on a slower but consistent decrease through the rest of the simulation. This change in rate can be explained by considering the Ca-C binding probabilities as a function of time (Fig. S16 b). Around 10 ns, the probability of Ca^{2+} coordinating to three anions decreased while the binding of Ca^{2+} to single anions increased, with the relatively compact cluster "opening" to maximize ion solvation and converting to a system dominated by free ions and ion complexes.

The simulations showed that clusters continued to decrease in size. At the end of the trajectory 70% of all associated species were ion pairs, and in the last 2 ns the largest sampled cluster contained four ions (Fig. S16 c, Fig. S16 d and Table S7). In addition, a number of ion trimers were sampled which were more likely to be positively charged, while also negatively charged trimers were found in earlier stages of the trajectory. As for systems at basic pH, there was a small probability of finding clusters up to the maximum of $R_g \approx 0.4$ nm. Combined, the data suggest that in homogeneous solution, the distribution of cluster sizes follows what is predicted from classical concepts of nucleation. Any liquid-like large clusters in solutions will tend to dissolve, but the kinetics associated with dissolution will be slow.

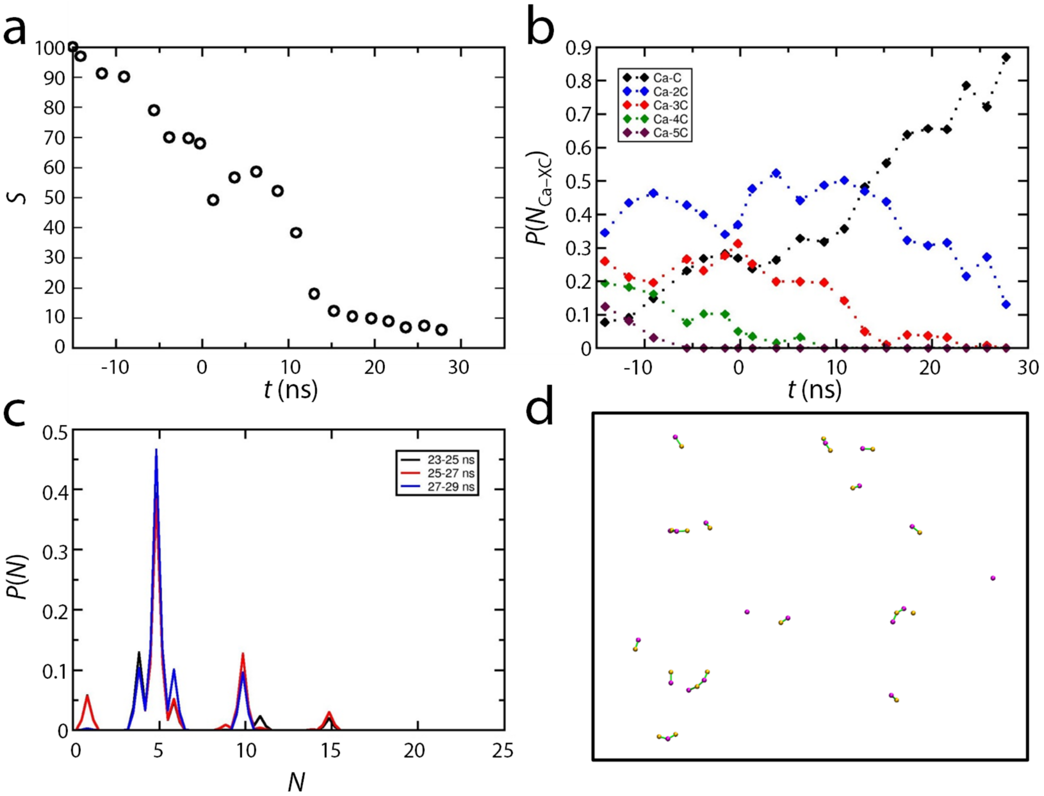

Figure S16. Dissolution of a 20 $CaCO_3$ cluster during 45 ns simulation at a concentration of 20 mM. **(a)** shows the average mass weighted cluster size, *S*, as a function of time. **(b)** gives the average coordination probabilities of *X* carbons to bind to calcium ($P(N_{Ca\text{–}XC})$) over time; **(c)** shows the cluster size probability distributions (here *N* is the number of atoms in a cluster) calculated in 2 ns windows from the final 6 ns of simulation with Gaussian kernel smoothing. Note that a single ion pair of $CaCO_3$ consists of 5 atoms. **(d)** Shows a snapshot (with oxygen and hydrogen omitted) from the final 2 ns of simulation (see Fig. S14 for key).

Table S7. Probability of observing distinct ionic species containing n_{Ca} calcium and n_{Carb} carbonate ions during the final 2 ns of a 45 ns simulation of a $Ca(CO_3)_{20}$ cluster.

$\boldsymbol{n_{Ca}}$	$\boldsymbol{n_{Carb}}$	***P***
1	1	0.70
2	1	0.15
2	2	0.15

3.3 Simulations at High Supersaturation: DLP Formation

During the initial stages of $CaCO_3$ precipitation from homogeneous solution, microscopic regions of ion-rich solution will form. Moreover, addition of the titrant to the analyte solution will induce transient local high ion concentrations. Hence, understanding the solution equilibrium at high supersaturation is essential to elucidate the mechanisms of mineral formation. To this end, three random systems were simulated containing 100 (0.57 M), 200 (1.1 M) and 300 (1.7 M) free Ca^{2+} and CO_3^{2-}, respectively, in 10,000 water molecules (Materials and Methods 1.10, Table S2). 60 ns MD simulations were performed at 298 K and 1 atm, before 10 ns production runs were conducted at constant volume. Equilibrium averages and system properties were measured from the final 5 ns of the latter simulation.

3.3.1 Phase Separation

In all three systems, ion association was observed very early in the trajectory and clusters grew and aggregated to give large associates which incorporated the majority of available ions (Fig. S17 and Table S8). At 0.57 M a nanoparticle was evident in solution in equilibrium with a number of free ions and smaller ion associates. At higher concentrations, the large cluster that formed percolated the periodic boundaries of the simulation cell to form a cluster of infinite size (Fig. S17). With periodic boundaries, a cylindrical geometry offers the minimum surface energy for phases in solution above a certain size: assuming perfect spheres and cylinders for clusters, there will be a crossover in the minimum surface energy from a sphere to an infinite cylinder when the radius of the sphere exceeds $L/3$ (or the radius of the cylinder $2L/9$) where L is the simulation cell length. For all three random systems, L = 6.7 nm and so this cross-over would occur for a sphere of radius around 2.2 nm, or cylinder with radius 1.6 nm. These values are for perfect geometries with sharp interfaces, whereas the surface of the particle at 0.57 M, and cylinder at 1.1 and 1.7 M, is clearly diffuse (see Fig. S23 for details). Nevertheless, the variation in density with distance from the particle center of mass suggest that radii of 1.5–2 nm for the particle (Fig. S21 a), and 1.3–1.7 nm for the cylindrical system (Fig. S21 b and Fig. 5 e main text), are sufficiently similar to these limits to suggest that these may be the same state, and that surface tension is driving the change of particle shape. This is further supported by the fact that the enthalpy of ionic clusters in the three systems is very similar, with a small decrease as the clusters get bigger, and hence the interfacial energy becomes a smaller component of the overall energy (Table S9). That change in enthalpy is concomitant with the change in water content (see Section 3.3.3 for details) in the first solvation shell of ions in the largest clusters.

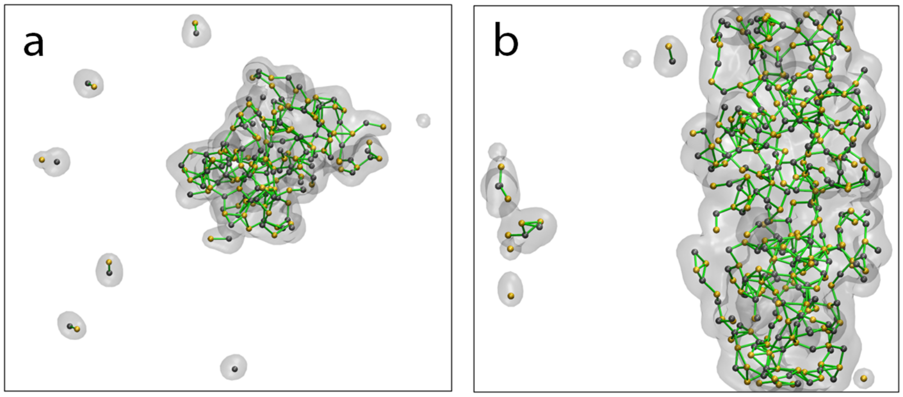

Figure S17. Snapshots taken from the final portion of simulations of $CaCO_3$ random solutions at **(a)** 0.57 M and **(b)** 1.1 M. Ions aggregate in solution to form a large cluster, in equilibrium with a lean ionic solution of free ions, ion pairs and smaller ion associates. For the highest concentrations, the large cluster percolated through the periodic boundaries of simulation cells to form an infinitely large ionic network, as can be seen in (b). Calcium and carbon are shown as gold and grey, respectively. Green lines indicate connections between ion centers where $r_{Ca\text{–}C} \leq 4.2$ Å. A transparent surface for calcium and carbonate is shown as a van der Waals radius.

Table S8. Fraction of ions in the largest cluster

	0.57 M	**1.1 M**	**1.7 M**
Ions in the largest cluster	87 %	96 %	93 %

Table S9. Enthalpy of ions, H_{ions}, per $CaCO_3$ unit, N_{CaCO_3}. Uncertainties are one standard deviation.

	0.57 M	**1.1 M**	**1.7 M**
$\frac{H_{ions}}{N_{CaCO_3}}$ (eV)[1]	–29.41 ± 0.02	–29.74 ± 0.01	–29.85 ± 0.01

For all three systems, the cluster size probability distributions showed a peak at large number of ions, N_{ions} (Fig. S18). These peaks are broad due to the dynamic nature of ion coordination and the fluctuating size of the clusters on the timescale of the simulations. Visual inspection confirmed dynamic (dis)ordering in clusters and showed that ions had relatively high mobility (see Section 3.4 for more details), consistent with a liquid. Surrounding the large clusters were a small number of predominantly free ions and ion pairs, and

---

[1] The enthalpy of bulk water, H_{BW}, was subtracted from the total enthalpy of the system, H, to calculate the enthalpy of solvated ions, $H_{ions} = H - H_{BW}$. The enthalpy of bulk water at equilibrium was measured, and $H_{BW} = N_W H_{Wat}$ where H_{Wat} is the average enthalpy per bulk water molecule and N_W are the number of water molecules in the simulation cell of interest.

occasionally larger ion associates (Fig. S17 and Fig. S18) up to around N_{ions} = 10. At 1.1 M, there is a low probability of finding clusters with a radius of gyration < 0.4 nm (Fig. S19), consistent with the results at basic pH and low concentration. Hence, in all high supersaturation systems phase separation occurred between a dense liquid, rich in calcium carbonate, and a lean liquid comprising an aqueous solution containing free ions and ion pairs. As this happens spontaneously in simulations, it is likely that any energy barrier to phase separation is smaller than a few k_BT at these high concentrations. It is not clear from simulations whether there is indeed a small energy barrier, as expected for a binodal phase separation at such high concentrations, or whether there is no energy barrier, indicative of spinodal decomposition.

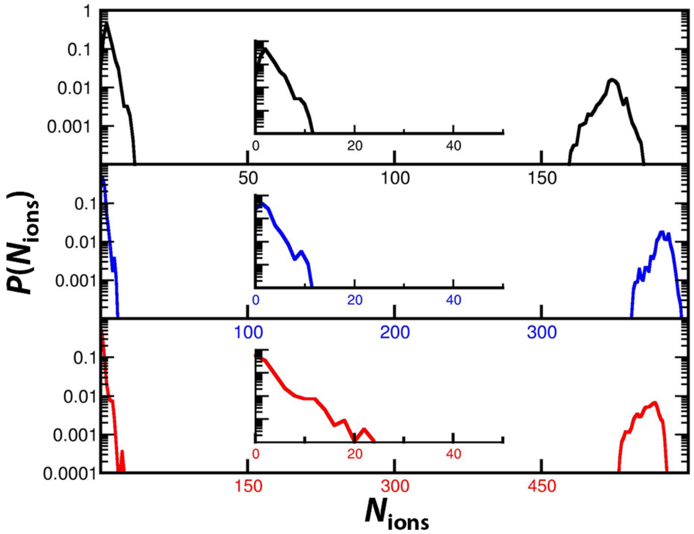

Figure S18. Cluster size probability distributions for clusters emerging in solutions at 0.57 (black), 1.1 (blue) and 1.7 M (red). Sizes are plotted for clusters as a function of number of ions, N_{ions}. Inset are the same distributions up to a maximum of N_{ions} = 50.

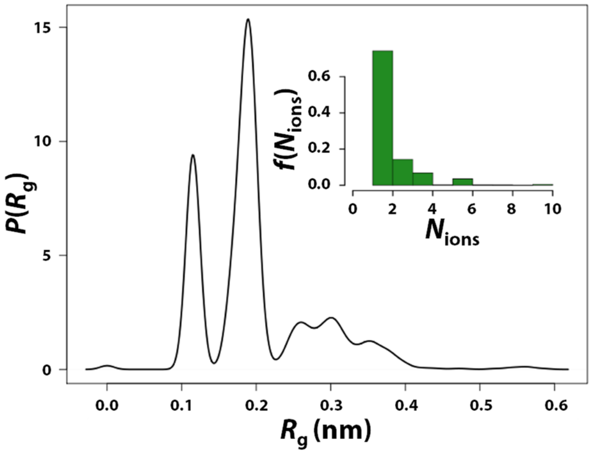

Figure S19. Ion associates in lean solution. Probability density *P* of the radius of gyration, R_g, for free ions and small ion associates at equilibrium in a system with an initial free ion concentration of 0.57 M. Inset: histogram number of ions per cluster in N_{ions}.

3.3.2 Dense Liquid Structure

The dynamic nature of ion coordination is reflected by the probability densities for the lifetime of cation-anion “bonds” in Fig. S20 b. Bond breaking was prolific during simulation. Short bond lifetimes, where coordination lasts no more than about 100 ps, were highly probable with around 70% of connections breaking on this time scale. However, other ionic connections lasted much longer, with comparable probabilities at all concentrations for bond breaking on the time scale of nanoseconds, up to the maximum time of 5 ns. A small fraction of bonds (less than 10%) remained intact during the whole simulation. Visual inspection showed that reconfiguration of the ionic network is faster at the interface with lean solution, with connections in the core of the dense liquid remaining for longer times.

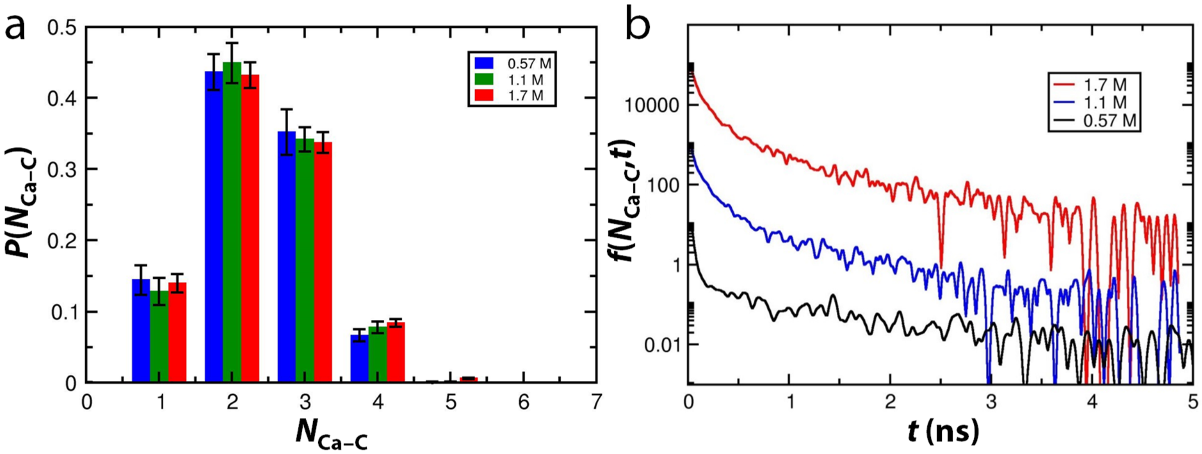

Figure S20. **(a)** Coordination probabilities for calcium to bind to $N_{\text{Ca–C}}$ carbons in systems at high concentration. Probabilities P were measured for all associated ions and error bars show uncertainties of one standard deviation in the distribution. **(b)** Probability densities for Ca–C bond lifetimes in clusters; bonds were defined by a distance cutoff of 4.2 Å, and were sampled from the final 5 ns of simulation. Data for 1.1 and 1.7 M have been shifted by two and four orders of magnitude, respectively, to make the plot clear. The data was smoothed using a running average over ten data points.

The radial density for ions and water from the core of dense liquids with initial concentrations of 0.57 and 1.7 M is shown in Fig. S21 a and b, respectively. As mentioned above, the interface between the dense liquid and aqueous solution is diffuse, with ion densities tailing from the maximum to zero over approximately 1 nm. The ionic density at small radii show a lot of scatter, due to the small finite number of ions involved; nonetheless, the molar mass density in the core can be estimated to be 970–1150 kg m^{-3}. Water density in the core of DLP (ρ = 880–1000 kg m^{-3}) was quite close to that in the lean solution, which in turn is equal to the density of bulk water (simple point charge/flexible model water (SPC/Fw)(8); 1012 kg m^{-3}). For comparison, the ion and water densities in bulk amorphous $CaCO_3 \cdot H_2O$ were measured to be 2660 and 400 kg m^{-3}, respectively. Fig. S21 c,d (and Fig. 5 f main text) show the coordination of calcium with anions and water as a function of radius from the core of dense liquid regions. A general trend can be observed: as the distance from the center of mass is increased, there is a corresponding decrease in ionic coordination and an increase in ion hydration. In the core of the DLP, Ca–OC coordination is around 6 with a small number of water molecules binding to cations. At the periphery of the dense liquid we find ionic coordination numbers of one, and cations are almost fully solvated in the first shell.

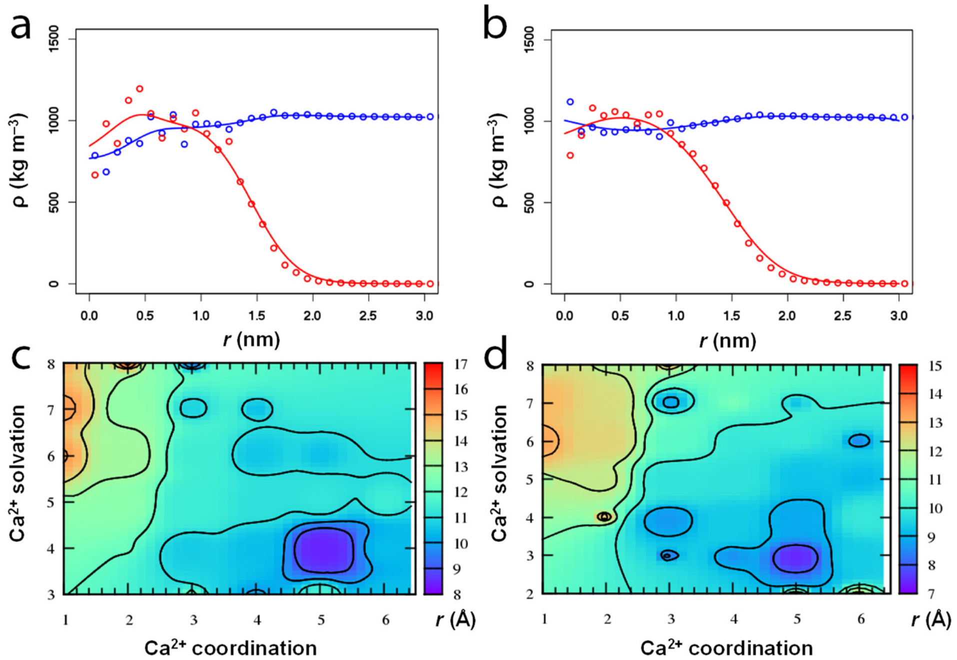

Figure S21. Top: mass densities, ρ (in kg m^{-3}) of ions (red) and water (blue) as a function of distance from the center of mass (in terms of ions), *r*, of dense liquids in systems with initial concentration: **(a)** 0.57 M and **(b)** 1.7 M. Data points were averaged over the trajectory and lines were generated using Gaussian kernel regression with a bandwidth of 0.6 nm. Bottom: coordination probability maps generated from interpolated data for **(c)** 0.57 M and **(d)** 1.7 M systems at equilibrium. Ca^{2+} coordination numbers in the first coordination shell (measured according to the first minimum in radial distribution functions, for details see Materials and Methods 1.11) to carbonate oxygen atoms, Ca^{2+} coordination, and water, Ca^{2+} solvation, are plotted with the distance of calcium from the center of mass highlighted by the map color on the right (scale in Å).

3.3.3 Water in the Dense Liquid Phase

A snapshot below the surface of the DLP in Fig. S22 shows a significant amount of water percolating through an ionic network. While water exchange with lean solution does take place on the timescales of the simulation, a significant amount of water in the core of the dense liquid remains tightly bound to ions over the course of nanoseconds. Water networks in the core, defined by a distance criteria (guided by position of the minimum following the first peak in water O–O radial distribution functions (RDFs)), were stable during simulation, and so this structural water is different from solvating water molecules which can be found surrounding ions in bulk lean solution.

The number of water molecules in the first coordination shell of ions in the DLP found in the three high concentration systems are listed in Table S10. The data are for ions which are within 9 Å of the center of mass of the DLP. Close to the center of mass the amount of water approached roughly ~4 water molecules per $CaCO_3$, while at the periphery of the dense liquid there are around ~7 water molecules per $CaCO_3$ unit. Hence, we generally describe a stoichiometric ratio of 4–7 $H_2O/CaCO_3$ for the DLP.

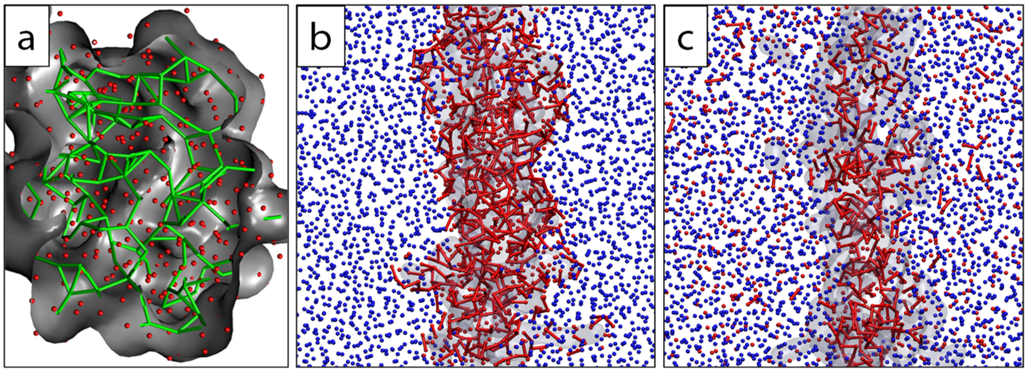

Figure S22. **(a)** Snapshot of the large cluster at 0.57 M. A solid surface for calcium carbonate is shown in grey, constructed using van der Waals radii. A slice through the surface reveals connections between calcium and carbon atoms, shown as green bonds where $r_{\mathrm{Ca-C}} \leq 4.2$ Å. Red spheres show water oxygen atoms within 3.2 Å of ions. **(b)** and **(c)** show snapshots of a slice through the simulation cell z axis of a system at 1.1 M showing the percolating dense liquid (as a transparent grey surface) at (b) $t = 0$ and (c) $t = 5$ ns. Water within 3.2 Å of ions at t = 0 is shown in red, with lines showing water connections within 3.5 Å, while all other water is shown in blue.

Table S10. Water molecules per ion in the first solvation shell of ions in the core of dense liquids. Water within 3.2 Å of Ca and 4.5 Å of C was used in the calculations, as these represent the first minimum in Ca-O_{wat} and C-O_{wat} radial distribution functions, respectively.

	0.57 M	**1.1 M**	**1.7 M**
H_2O per ion	4.27 ± 0.1	3.48 ± 0.09	3.51 ± 0.09

3.4 Simulations of the DLP: Ion Mobility

The mean squared displacement (MSD) of ions in DLP was measured for Ca and C. These were calculated as a function of radial distance from the center of mass of DLP clusters in three dimensions (3D), while for the infinite DLP cylindrical networks this was measured in 2D for segments of the cylinder. In order to distinguish between diffusion within the DLP and collective diffusion of the DLP, the translational motion of the cluster was removed from the calculation of the MSD (see Materials and Methods 1.11). The MSD for calcium in DLP radial windows at 0.57 M is shown in Fig. S23. It is clear that the mobility of ions increases with increasing radius. This is not surprising as the ionic coordination of ions decreases away from the core of the DLP, and the increased ion hydration in the diffuse interface allows greater ion translational motion.

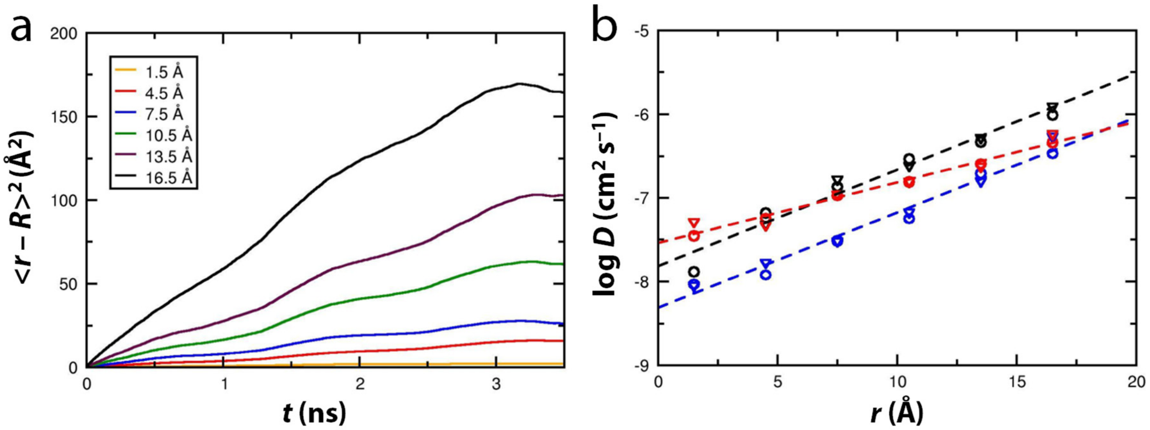

Figure S23. **(a)** Internal mean squared displacement, <r–R>^{2}, for ions in different radial spheres from the cluster center of mass in the dense liquid nanoparticle which emerged in simulations at 0.57 M. **(b)** The logarithm of internal ion diffusion is shown as a function of radius from the center of mass of dense liquids with initial concentration 0.57 (black), 1.1 (blue) and 1.7 M (red). Data for calcium is shown as circles, with the carbon of carbonate shown as triangles. Linear fits through the data for ions at different concentrations are shown. D was calculated from mean squared displacements at t = 0.1–1.6 ns.

Diffusion coefficients were calculated from the slope of the linear portions of the MSDs and are shown in Fig. S23. The trends for increasing *D* at larger radius are consistent for the two lower concentration phases. These also show comparable radial density profiles out to about 20 Å (Fig. S21). The highest concentration system (1.7 M) shows a more gradual change in diffusion coefficient with distance from the center of the DLP, which is consistent with the larger cylinder radius observed in this system. For ions within 6 Å of the center of the DLP particles, diffusion coefficients were ~10^{-8} cm^2 s^{-1} (diffusion of ions in bulk amorphous $CaCO_3 \cdot H_2O$ was measured to be ~10^{-10} cm^2 s^{-1}) which is considerably smaller than diffusion coefficients typical of most liquids (10^{-6}–10^{-5} cm^2 s^{-1}). In the interfacial regions, *D* was 10^{-6}–10^{-7} cm^2 s^{-1}, and approaching the values for dissolved ions. The diffusion in these bulk systems is smaller than was found by Wallace *et al.* (39); in part this will be because of the much larger DLP particles in this study, but is also likely to arise from the removal of collective particulate motion from the calculated diffusion coefficients.

3.5 TEM Simulations of Dense Liquids

3.5.1 Defocus Sensitivity Analysis

TEM image simulation requires many input parameters. In the case of the current work, the defocus has been highlighted as being crucial to determining the relative phase contrast of objects in TEM and to observe nanoparticles in solution before nucleation. Indeed, aside from the defocus, the microscope parameters we adopted were as close as possible to those used in experiments. In simulations, the Scherzer defocus was used, representing an underfocus of 0.087 µm (a positive underfocus represents a negative defocus), whereas the underfocus in experiments was 0.5 μm. The smaller underfocus was used to retain the necessary resolution in the simulations. It is, therefore, important to test the sensitivity of this parameter to the measured relative image contrast of dense liquids compared to lean ionic solutions.

The final configuration from 1.7 M MD simulations was used to generate a ~130 nm deep sample for TEM simulations. The sample was oriented such that the electron beam was parallel to dense liquid and lean solution regions which filled the entire sample. This ensured that average electron intensities could be measured at the detector for DLP and lean solution regions. TEM simulations were performed with varying degrees of underfocus from 0 to 0.5 μm. All other input parameters remained the same (see Materials and Methods 1.12.5). Therefore, any change in the electron intensity in regions where the dense liquid was positioned, I_{DLP}, compared to that for the background solution, I_{sol}, were only due to the change in the defocus.

The measured relative image contrast of the DLP compared to the solution, I_{DLP} / I_{sol} are provided in table S11. There is a decrease of around 5 % in the relative image contrast measured. However, the average value of relative contrast even at 0.5 μm is still significantly higher than the measured image contrast of ACC nanoparticles (I_{DLP} / I_{sol} ≈ 67 %). Within one standard deviation, the relative image contrast of the DLP *vs*. background solution in simulations was the same. This shows that the method is robust in distinguishing between DLP and more dense systems in the current study.

Table S11. Relative phase contrast, I_{DLP} / I_{sol}, and electron intensities at the detector in regions of the DLP I_{DLP} for TEM simulations with varying values of underfocus.

Underfocus (μm)	**I_{DLP} (a.u.)**	**I_{DLP} / I_{sol}**
0	131 ± 6	0.87 ± 0.07
0.05	132 ± 6	0.87 ± 0.07
0.1	128 ± 7	0.84 ± 0.06
0.2	124 ± 10	0.82 ± 0.07
0.5	125 ± 12	0.82 ± 0.08

3.5.2 TEM of DLP and Lean Solution

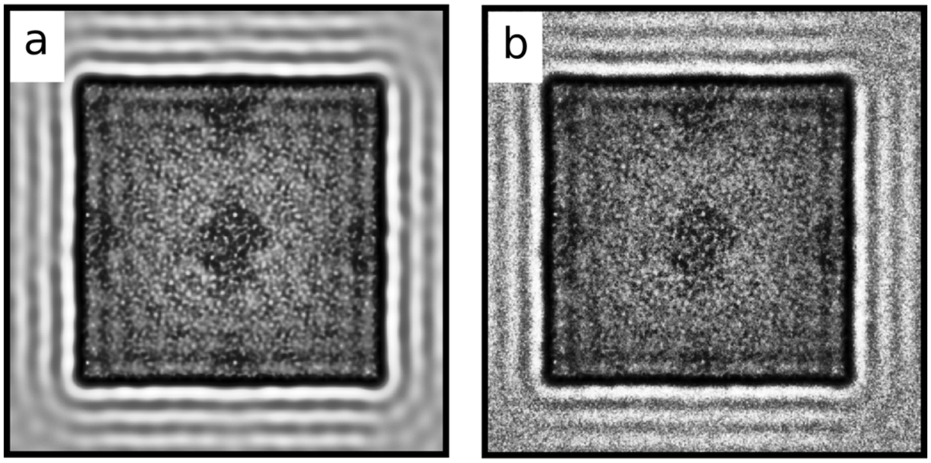

Figure S24. TEM images for a sample containing the system at 1.7 M. A 20 × 2 × 2 supercell of the system was created and positioned such that the direction of dense liquid percolation was parallel to the optical axis. **(a)** shows the image with detector quantization (noise) removed, and **(b)** shows the image with a level of detector noise. The contrast has been enhanced here for clarity.

Fig. S24 shows TEM images calculated from simulation (see Materials and Methods 1.12.4 for input parameters). The supercell can be observed as a central square in the images, with dark spots in the center and at the edge. The ion–rich phase can clearly be seen as the darker regions in the image, due to increased scattering of electrons and contrast compared with the lean solution. Electron intensity, detected following transmission through lean solution, was equal to that of pure SPC/Fw water within statistical uncertainty when the same simulation parameters were used. At the interface between the sample and the background (modeled on bulk water), electrostatic potential discontinuities lead to regions of high and low intensity (referred to as Fresnel fringes). In measuring contrast, it is therefore important to avoid comparing intensities of phases which are close to the interface. DLP intensities at their lowest are 85 ± 5 % of the lean solution, and this compares well with experimental measurements where the dense liquid TEM intensity was 90 ± 4% (mean ± standard deviation of the distribution) of the lean ionic solution (see also Fig. 4 c and Fig. 7 a main text).

4. Bibliography

1. Gebauer D, Völkel A, & Cölfen H (2008) Stable Prenucleation Calcium Carbonate Clusters. *Science* 322(5909):1819-1822.
2. Friedrich H, Frederik PM, de With G, & Sommerdijk NAJM (2010) Imaging of Self-Assembled Structures: Interpretation of TEM and Cryo-TEM Images. *Angew Chem Int Ed* 49(43):7850-7858.
3. Pouget EM*, et al.* (2009) The Initial Stages of Template-Controlled $CaCO_3$ Formation Revealed by Cryo-TEM. *Science* 323(5920):1455-1458.
4. Kellermeier M*, et al.* (2012) Colloidal Stabilization of Calcium Carbonate Prenucleation Clusters with Silica. *Adv Funct Mater* 22:4301-4311.
5. Demichelis R, Raiteri P, Gale JD, Quigley D, & Gebauer D (2011) Stable prenucleation mineral clusters are liquid-like ionic polymers. *Nat Commun* 2:590.
6. Finney AR & Rodger PM (2012) Probing the structure and stability of calcium carbonate pre-nucleation clusters. *Farad Discuss* 159(0):47-60.
7. Demichelis R, Raiteri P, Gale JD, Quigley D, & Gebauer D (2011) Stable prenucleation mineral clusters are liquid-like ionic polymers. *Nat Commun* 2:590.
8. Paesani F, Zhang W, Case DA, Cheatham TE, & Voth GA (2006) An accurate and simple quantum model for liquid water. *J Chem Phys* 125(18):184507.
9. Todorov IT, Smith W, Trachenko K, & Dove MT (2006) DL_POLY_3: new dimensions in molecular dynamics simulations via massive parallelism. *J Mater Chem* 16(20):1911-1918.
10. Humphrey W, Dalke A, & Schulten K (1996) VMD: Visual molecular dynamics. *J Mol Graphics* 14(1):33-38.
11. Rullgård H, Öfverstedt LG, Masich S, Daneholt B, & Öktem O (2011) Simulation of transmission electron microscope images of biological specimens. *J Microsc* 243(3):234-256.
12. Peng L-M, Ren G, Dudarev SL, & Whelan MJ (1996) Robust Parameterization of Elastic and Absorptive Electron Atomic Scattering Factors. *Acta Cryst A* 52(2):257-276.
13. Peng L-M (1998) Electron Scattering Factors of Ions and their Parameterization. *Acta Cryst A* 54(4):481-485.
14. Bushuev YG, Finney AR, & Rodger PM (2015) Stability and Structure of Hydrated Amorphous Calcium Carbonate. *Cryst Growth Des* 15:5269.
15. Kellermeier M, Picker A, Kempter A, Cölfen H, & Gebauer D (2014) A Straightforward Treatment of Activity in Aqueous $CaCO_3$ Solutions and the Consequences for Nucleation Theory. *Adv Mater* 26(5):752-757.
16. Metrohm AG (2013) *Manual for Ion-Selective Electrodes* (Herisau, Switserland).
17. Lide DR (1997) *CRC handbook of chemistry and physics : a ready-reference book of chemical and physical data* (CRC press, Boca Raton; New York).
18. Hasselbalch KA (1916) Die Berechnung der Wasserstoffzahl des Blutes aus der freien und gebundenen Kohlensäure desselben, und die Sauerstoffbindung des Blutes als Funktion der Wasserstoffzahl. *Biochem Z* 78:112-144.
19. Davies CW (1962) *Ion association* (Butterworths, Washington).
20. Hückel E (1924) Zur Theorie der Elektrolyte. *Ergebnisse der Exakten Naturwissenschaften: Dritter Band*, (Springer Berlin Heidelberg, Berlin, Heidelberg), pp 199-276.
21. Haider C (2013) *Electrodes in Potentiometry* (Herisau, Switzerland).

22. Hawley JE (1973) Bicarbonate and carbonate ion association with sodium, magnesium and calcium at 25 C and 0.72 ionic strength, *Limnol Oceanogr* 19(2):223-234.

23. Plummer LN & Busenberg E (1982) The solubilities of calcite, aragonite and vaterite in CO_2-H_2O solutions between 0 and 90°C, and an evaluation of the aqueous model for the system $CaCO_3$-CO_2-H_2O. *Geochim Cosmochim Acta* 46(6):1011-1040.

24. Bates RG & Vijh AK (1973) Determination of pH: Theory and Practice. *J Electrochem Soc* 120(8):263C.

25. Soli AL & Byrne RH (2002) CO_2 system hydration and dehydration kinetics and the equilibrium CO_2/H_2CO_3 ratio in aqueous NaCl solution. *Mar Chem* 78(2–3):65-73.

26. Sander R (1999) Compilation of Henry's Law constants for inorganic and organic species of potential importance in environmental chemistry. http://www.henrys-law.org/henry-3.0.pdf

27. Loerting T & Bernard J (2010) Aqueous Carbonic Acid (H_2CO_3). *ChemPhysChem* 11(11):2305-2309.

28. Felmy AR, Girvin DC, & Jenne EA (1984) *MINTEQ--a Computer Program for Calculating Aqueous Geochemical Equilibria: February 1984* (National Technical Information Service, U.S. Environmental Protection Agency, Washington D.C.).

29. Truesdell AH & Jones BF (1974) WATEQ, a computer program for calculating chemical equilibria of natural waters. *J Res US Geol Survey* 2:233-248.

30. Binder K (1983) Collective diffusion, nucleation, and spinodal decomposition in polymer mixtures. *J Chem Phys* 79(12):6387-6409.

31. Cahn JW & Hilliard JE (1958) Free Energy of a Nonuniform System. I. Interfacial Free Energy. *J Chem Phys* 28(2):258-267.

32. Cook HE (1970) Brownian motion in spinodal decomposition. *Acta Metall* 18(3):297-306.

33. Siggia ED (1979) Late stages of spinodal decomposition in binary mixtures. *Phys Rev A* 20(2):595-605.

34. Binder K & Stauffer D (1974) Theory for the Slowing Down of the Relaxation and Spinodal Decomposition of Binary Mixtures. *Phys Rev Lett* 33(17):1006-1009.

35. Wong N-C & Knobler CM (1981) Light-scattering studies of phase separation in isobutyric acid + water mixtures: Hydrodynamic effects. *Phys Rev A* 24(6):3205-3211.

36. Roux D (1986) Spinodal decomposition in microemulsions. *J Phys France* 47(5):733-738.

37. Bhat S, Tuinier R, & Schurtenberger P (2006) Spinodal decomposition in a food colloid–biopolymer mixture: evidence for a linear regime. *J Phys Condens Matter* 18(26):L339.

38. Zou Z*, et al.* (2017) On the Phase Diagram of Calcium Carbonate Solutions. *Adv Mater Interfaces* 4(1):1600076.

39. Wallace AF*, et al.* (2013) Microscopic Evidence for Liquid-Liquid Separation in Supersaturated $CaCO_3$ Solutions. *Science* 341(6148):885-889.